A Conserved Mycobacterial Nucleomodulin Hijacks the Host COMPASS Complex to Reprogram Pro-Inflammatory Transcription and Promote Intracellular Survival

Liu Chen[1,2], Baojie Duan[1], Pingping Chen[1], Qiang Jiang[1], Yifan Wang[1], Lu Lu[1], Yingyu Chen[1,3,4], Changmin Hu[1,3], Lei Zhang[1,3,4]* and Aizhen Guo[1,2,3,4]*

[1] National Key Laboratory of Agricultural Microbiology, College of Veterinary Medicine, Huazhong Agricultural University, Wuhan 430070, China

[2] Hubei Hongshan Laboratory, Huazhong Agricultural University, Wuhan 430070, China

[3] National Professional Laboratory for Animal Tuberculosis, Ministry of Agriculture and Rural Affairs, Huazhong Agricultural University, Wuhan 430070, China

[4] Hubei Jiangxia Laboratory, Wuhan 430207, China

*Address correspondence to: Lei Zhang, zhanglei2023@mail.hzau.edu.cn; Aizhen Guo, aizhen@mail.hzau.edu.cn

ABSTRACT

Nucleomodulins are a class of effector proteins secreted by bacterial pathogens that translocate into the host cell nucleus to modulate nuclear processes. However, their target proteins and underlying molecular mechanisms remain poorly understood in mycobacteria. Herein, we identified a conserved hypothetical protein Rv1075c, designated MgdE, as a nucleomodulin that enhances mycobacterial intracellular survival. MgdE undergoes nuclear translocation via two nuclear localization signals, KRIR$^{108-111}$ and RLRRPR$^{300-305}$, and interacts with ASH2L and WDR5, two subunits of the host histone methyltransferase COMPASS complex. This interaction suppresses histone H3 lysine 4 (H3K4) methylation-mediated transcription of pro-inflammatory genes, including *IL6* and *IL1B*, thereby promoting mycobacterial survival in both macrophages and mice. Our study provides the first experimental evidence that a bacterial nucleomodulin facilitates intracellular survival by directly targeting the host COMPASS complex. These findings advance our understanding of mycobacterial pathogenesis by revealing a novel mechanism that contributes to its intracellular survival strategy.

Keywords Mycobacteria; Nucleomodulin; Histone methyltransferase; Inflammatory genes; Pathogenesis.

INTRODUCTION

Nucleomodulins constitute a distinct class of bacterial proteins capable of translocating into the nuclei of eukaryotic cells, where they strategically modulate nuclear processes to promote pathogen survival and persistence (Radoshevich et al., 2018; Hanford et al., 2021). These

evolutionarily diverse effector proteins, secreted by distinct pathogens, exhibit remarkable adaptability in infiltrating host nuclei and reprogramming the transcriptional and epigenetic regulatory networks (Bierne et al., 2012; Bierne et al., 2020). Upon nuclear localization, nucleomodulins employ diverse molecular mechanisms to subvert host cellular processes, including but not limited to: (i) direct interactions with genomic DNA or nuclear proteins (Rennoll-Bankert et al., 2015; Sun et al., 2016; Prokop et al., 2017), (ii) hijacking post-translational modification systems (Lebreton et al., 2014; Rolando et al., 2023), (iii) dysregulating signaling molecule activity or localization (Zhao et al., 2019; Chambers et al., 2020; Evans et al., 2018), and (iv) destabilizing nuclear architecture (Pourpre et al., 2022; Fu et al., 2021). Specific examples include AnkA, a bacterial protein from *Anaplasma phagocytophilum,* which binds to specific A/T-rich sequences in the host cell, alters chromatin architecture, and modulates gene transcription (Rennoll-Bankert et al., 2015). In *Listeria monocytogenes*, LntA interacts with the proline-rich domain of BAHD1, to disrupt BAHD1-mediated gene silencing and promote histone H3 acetylation (Lebreton et al., 2014). Another example is OspF from *Shigella flexneri*, which exploits its phosphothreonine lyase activity to irreversibly dephosphorylate MAPKs, thereby preventing the transcriptional activation of NF-κB-regulated genes (Chambers et al., 2020). Unlike these effectors, *L. monocytogenes* InlP takes a different approach by hijacking the splicing factor RBM5. This interaction not only suppresses apoptosis but also reorganizes nuclear speckles through SC35 redistribution and RBM5-dependent granule formation (Pourpre et al., 2022). These examples illustrate the diverse and sophisticated mechanisms used by nucleomodulins to reprogram host nuclear functions, ultimately manipulating the intracellular environment to their advantage.

The evolutionary refinement of nucleomodulins is exemplified by their ability to exploit chromatin-based regulatory systems, with histone methylation emerging as a pivotal axis in host–pathogen interactions (Bierne et al., 2020; Khan et al., 2021). As a central epigenetic modification, histone methylation dynamically controls chromatin accessibility and transcriptional outcomes (Yu et al., 2024; Wang et al., 2025). By precisely targeting specific histone residues, nucleomodulins reprogram chromatin states to either suppress host immune responses or promote cellular pathways conducive to pathogen survival (Lebreton et al., 2014; Schator et al., 2023; Rolando et al.,2023; Denzer et al., 2020). A paradigm of this molecular strategy is demonstrated by the *Chlamydia trachomatis* nuclear effector NUE, which utilizes its conserved SET domain to catalyze the methylation of histones H2B, H3, and H4, establishing a repressive chromatin state that downregulates antimicrobial gene expression (Fol et al., 2020). Similarly, RomA uses its ankyrin and SET domains to bind and methylate histone H3, thereby altering the host chromatin to enhance *Legionella* intracellular survival (Schator et al., 2023; Rolando et al., 2013). *Legionella* LegAS4 catalyzes H3K4 methylation to promote an open chromatin state, enhancing ribosomal RNA transcription and facilitating bacterial intracellular replication (Denzer et al., 2020). These cases emphasize how pathogens exploit histone methylation as a molecular lever to hijack the host epigenetic machinery.

Mycobacterium tuberculosis (Mtb), the causative agent of tuberculosis, is a highly successful pathogen because of its ability to survive within macrophages, evade the immune system, and persist in the host, ultimately leading to a chronic disease state (Chandra et al., 2022; Chai et al., 2020). Central to its pathogenic strategy is the secretion of a diverse array of effector proteins (Chai et al., 2022; Bates et al., 2024; Qiang et al., 2023), including

66 nucleomodulins that subvert host nuclear processes. The tyrosine phosphatase PtpA
67 exemplifies this strategy by directly binding to the promoter regions of immune-related genes,
68 including *GADD45A*, to suppress innate immune responses (Wang et al., 2017). The
69 methyltransferase Rv1988 mediates an unconventional histone modification by methylating
70 histone H3 at arginine 42 (H3R42me), thereby silencing antimicrobial defense mechanisms
71 (Yaseen et al., 2015). Similarly, the acetyltransferase Rv3423.1 modulates chromatin
72 accessibility through acetylation of histone H3 at lysine 9 and 14 (H3K9/K14ac), attenuating
73 pro-inflammatory signaling pathways (Jose et al., 2016). Rv2966c represents a unique
74 bacterial DNA methyltransferase that establishes non-canonical CpG methylation patterns to
75 epigenetically silence host immune-related gene expression (Sharma et al., 2015). Despite
76 these molecular insights, the comprehensive landscape of the nuclear effector systems of Mtb,
77 particularly the mechanistic details of nucleomodulin interactions with host chromatin-
78 modifying complexes and their spatiotemporal regulation during infection, remains poorly
79 defined. This critical knowledge gap impedes our understanding of how Mtb coordinates
80 system-level transcriptional rewiring in the host cellular environment.

81 In this study, we utilized bioinformatics analysis combined with fluorescence imaging to
82 rapidly screen for potential nucleomodulins in pathogenic mycobacterial species. Using this
83 approach, the hypothetical protein Rv1075c (designated as MgdE) was identified and
84 subsequently validated. MgdE undergoes nuclear translocation mediated by two nuclear
85 localization signals, $KRIR^{108-111}$ and $RLRRPR^{300-305}$, and interacts with the histone
86 methyltransferase COMPASS complex subunits ASH2L and WDR5. This interaction
87 suppresses H3K4me3-mediated inflammatory gene expression, thus dampening host immune

88 responses and enhancing bacterial survival in macrophages and murine infection models. Our
89 findings identify MgdE as a nucleomodulin that targets the COMPASS complex, revealing a
90 novel epigenetic strategy exploited by mycobacteria for intracellular survival.

91 **RESULTS**

92 **Functional screening of potential nucleomodulins in pathogenic mycobacterial species**

93 To identify conserved nucleomodulins in pathogenic mycobacteria, we first conducted a pan-
94 genomic comparative analysis across four relevant species, including *M. tuberculosis* H37Rv
95 and H37Ra, *M. bovis* BCG, *M. marinum*, and *M. avium*, to categorize the core genes.
96 Subsequently, a dual-threshold screening approach was employed to predict the classical and
97 non-canonical secreted proteins encoded by these shared genes using SignalP 5.0 and
98 SecretomeP 2.0, with thresholds set at a D-score ≥0.5 (Hammond et al., 2018) and a neural
99 network (NN) score ≥0.9 (Bendtsen et al., 2005) (Table S1). This analysis yielded 135 high
100 confidence secreted protein candidates. Further analysis of these candidates nuclear
101 localization signal (NLS) motifs using cNLS Mapper (NLS score ≥2) identified 56 proteins
102 containing at least one putative NLS (Table S2). Following systematic classification based on
103 secretion machinery dependencies, the candidate proteins were categorized into four distinct
104 pathways: 26 Sec/SPI (signal peptide-driven), 7 Tat/SPI (twin-arginine translocase pathway),
105 18 Sec/SPII (lipoprotein-targeted), and 5 unclassified candidates lacking canonical secretion
106 motifs (Figure 1A and B, Figure S1A and B). Functional validation of nuclear trafficking was
107 conducted through the heterologous expression of enhanced green fluorescent protein
108 (EGFP)-tagged constructs in HEK293T cells, followed by quantitative profiling of the
109 subcellular distribution using laser scanning confocal microscopy (LSCM). Among them, six

110 Tat/SPI-associated proteins including Rv0519c, Rv0846c, Rv0945, Rv1075c/MgdE, Rv1291c
111 and Rv2577 (Table S3) exhibited nuclear localization and MgdE exhibited distinct nuclear
112 aggregation (Figure 1C). Nucleomodulins are effector proteins secreted by pathogens that
113 translocate into the host cell nucleus to modulate host functions. To examine whether MgdE
114 is secreted by mycobacteria, recombinant *M. bovis* BCG strains expressing C-terminally Flag-
115 tagged MgdE were constructed. Immunoblotting showed that MgdE and the secreted antigen
116 Ag85B were present in both cell pellets and culture supernatants, while the cytoplasmic protein
117 GlpX as the negative control was only detected in the cell pellets (Figure S2A), indicating that
118 MgdE is indeed secreted by *M. bovis* BCG. Collectively, these results suggest that MgdE might
119 be a potential nucleomodulin in the pathogenic mycobacteria.

120 **MgdE translocates into the host nucleus through its dual NLS**

121 MgdE is a putative GDSL-like lipase characterized by conserved esterase sequence motifs,
122 with the GDSx motif containing a nucleophilic Ser residue as part of block I (equivalent to the
123 classical G-x-S-x-G motif of lipases/esterases), and the consensus amino acids Gly, Asn, and
124 His located in blocks II, III, and V, respectively (Yang et al., 2019). Phylogenetic analysis
125 across the mycobacterial species revealed strict evolutionary conservation of MgdE, with most
126 strains encoding two predicted NLS: KRIR$^{108\text{-}111}$ (NLS1) and RLRRPR$^{300\text{-}305}$ (NLS2) (Figure 2A
127 and B). To further investigate the nuclear translocation capability of MgdE, HEK293T cells
128 were transfected with MgdE-EGFP, and its subcellular localization was examined at multiple
129 time points post-transfection. Confocal microscopy revealed a time-dependent increase of
130 MgdE-EGFP in the nucleus by 48 hours post-transfection (Figure S2B and C). To
131 quantitatively assess this process, MgdE expression and nuclear enrichment were analyzed

132 by cell fractionation and immunoblotting. These results demonstrated that MgdE protein levels
133 increased over time and progressively accumulated in the nucleus, consistent with the
134 confocal imaging observations (Figure S2D–E). Taken together, these experiments indicate
135 that MgdE is an evolutionarily conserved mycobacterial nucleomodulin with nuclear
136 translocation capacity.

137 To dissect the functional contributions of the predicted NLS motifs, EGFP-tagged NLS
138 deletion mutants including MgdE$^{\Delta NLS1}$, MgdE$^{\Delta NLS2}$, and MgdE$^{\Delta NLS1\text{-}2}$ were constructed and
139 transfected into HEK293T cells. Fluorescence intensity profiling revealed that individual
140 deletion of either NLS1 or NLS2 partially reduced the nuclear targeting efficiency, whereas
141 simultaneous deletion of both the NLS motifs (MgdE$^{\Delta NLS1\text{-}2}$) completely abrogated its nuclear
142 localization (Figure 2C and D). These observations were further confirmed by immunoblot
143 analysis of nuclear fractions, which showed that at 36 h post-transfection, MgdE-EGFP and
144 its mutant variants were consistently detected in the cytoplasmic compartment, and nuclear
145 accumulation of MgdE$^{\Delta NLS1\text{-}2}$ was nearly undetectable compared to that of MgdE (Figure 2E,
146 Figure S2F). To determine whether MgdE translocates into the host nucleus during
147 mycobacterial infection, recombinant BCG strains expressing Flag-tagged MgdE variants
148 were constructed, including single and double NLS deletion mutants (BCG/MgdE$^{\Delta NLS1}$-Flag,
149 BCG/MgdE$^{\Delta NLS2}$-Flag, and BCG/MgdE$^{\Delta NLS1\text{-}2}$-Flag). THP-1 macrophages were infected with
150 the recombinant strains, followed by subcellular fractionation. Nuclear-cytoplasmic
151 fractionation experiments showed that WT MgdE and the NLS single mutants could be
152 detected both in the cytoplasm and in the nucleus by immunoblotting, while the double mutant
153 MgdE$^{\Delta NLS1\text{-}2}$ was detectable only in the cytoplasm (Figure 2F). These results indicate that

154 MgdE translocates into the host nucleus via a dual NLS mechanism, with both NLS1 and NLS2
155 required for efficient nuclear import.

156 **Nuclear localization of MgdE enhances mycobacterial intracellular survival within**
157 **macrophages**

158 Given that MgdE exhibits nuclear translocation ability, we sought to determine whether this
159 ability plays a role in bacterial survival during infection. We generated various recombinant *M.*
160 *bovis* BCG strains, including wild-type BCG (WT), a *mgdE* deletion mutant (ΔMgdE) (Figure
161 S3A and B), ΔMgdE complemented with WT *mgdE* (Comp-MgdE), and ΔMgdE complemented
162 with NLS-deleted variant (Comp-MgdE$^{\Delta NLS1\text{-}2}$). All strains exhibited similar growth in 7H9 liquid
163 media supplemented with OADC (Figure S3C). To assess intracellular survival, we infected
164 THP-1 macrophages with each strain and monitored bacterial burden over time. As shown in
165 Figure 3A, the ΔMgdE mutant strain exhibited significantly reduced survival compared to the
166 WT strain, with accelerated bacterial clearance over time. This defect was rescued in the
167 Comp-MgdE strain, with intracellular survival levels restored to that in the WT strain. Notably,
168 the Comp-MgdE$^{\Delta NLS1\text{-}2}$ showed bacterial clearance equivalent to that in the ΔMgdE strains.
169 These results were consistent with the infection experiments using RAW264.7 macrophage
170 (Figure 3B). Furthermore, THP-1 macrophages infected with the ΔMgdE mutant strain
171 exhibited significant upregulation of inflammatory cytokines, including *IL1B*, *IL6*, *IL10,* and the
172 colony-stimulating factors *CSF1*–*CSF3* compared to the macrophages infected with the WT
173 strain (Figure 3C–H). Collectively, these results demonstrated that (i) MgdE enhances
174 mycobacterial intracellular survival and suppresses host inflammatory responses during
175 infection, and (ii) both NLS1 and NLS2 motifs are essential for the nuclear trafficking-

176 dependent function.

177 **MgdE physically interacts with the host COMPASS complex subunits ASH2L and WDR5**

178 To identify the potential host target proteins of MgdE, we employed AlphaFold to predict the
179 interactions between MgdE and majority of the nuclear proteins in the host. The prediction
180 results showed that MgdE binds to WDR5, a core component of the histone methyltransferase
181 COMPASS complex, with high confidence (pLDDT = 0.77) (Figure S4A and B). To
182 experimentally validate this prediction, we performed yeast two-hybrid (Y2H) assays. The
183 yeast cells co-expressing MgdE with either ASH2L or WDR5 exhibited robust growth on
184 selective SD/-Trp-Leu-His-Ade medium, whereas the cells co-expressing MgdE with DPY30
185 or RbBP5 showed no detectable growth, indicating specific interactions between MgdE and
186 ASH2L/WDR5 (Figure 4A). Further, these interactions were validated by co-
187 immunoprecipitation (Co-IP) assays. HEK293T cells were co-transfected with Flag-tagged
188 MgdE and HA-tagged ASH2L, WDR5, or RbBP5. The results revealed that HA-tagged ASH2L
189 and WDR5, but not RbBP5, co-precipitated with Flag-tagged MgdE (Figure 4B). Conversely,
190 Flag-tagged MgdE precipitated HA-tagged ASH2L and WDR5, but not RbBP5 (Figure 4C).
191 Taken together, these results demonstrate that MgdE specifically interacts with the
192 COMPASS complex subunits ASH2L and WDR5.

193 **The conserved residues D^{224} and H^{247} are critical for mediating the binding of MgdE to**
194 **WDR5**

195 To further confirm the interactions between MgdE and WDR5/ASH2L, the key amino acids of
196 MgdE (S^{80}, D^{244}, and H^{247}) were individually replaced with alanine (A) (Yang et al., 2019). The

197 Y2H assays showed that single-residue substitutions of MgdE did not affect its interaction with
198 ASH2L or WDR5. However, the $D^{244}A/H^{247}A$ double mutation specifically abrogated its
199 interaction with WDR5 but retained its ASH2L binding ability (Figure 5A). These findings were
200 further confirmed by Co-IP assays in HEK293T cells. Flag-tagged MgdE precipitated HA-
201 tagged ASH2L and WDR5 but not RbBP5, with reciprocal pull-downs confirming bidirectional
202 binding specificity. The $D^{244}A/H^{247}A$ double mutant maintained its interaction with ASH2L but
203 failed to bind WDR5, suggesting that these interactions are mediated through distinct
204 molecular interfaces (Figure 5B, Figure S4C). To further investigate the functional
205 consequences of these mutations, we analyzed the subcellular localization of the MgdE
206 mutants in transfected HEK293T cells using fluorescence co-localization assays. Wild-type
207 MgdE exhibited distinct nuclear aggregation over time, a phenomenon that was abrogated
208 following transfection with the $D^{244}A/H^{247}A$ mutant (Figure 5C), suggesting that the double
209 mutation impairs MgdE activity.

210 Given that MgdE interacts with WDR5, a subunit of COMPASS complex, which is a key
211 regulator of H3K4me3 methylation (Deng et al., 2024), we sought to determine whether this
212 interaction contributes to an epigenetic regulatory mechanism that facilitates bacterial
213 persistence within host cells. HEK293T cells were transfected with EGFP-tagged wild-type
214 MgdE (WT), the catalytic mutant MgdE-$D^{244}A/H^{247}A$, or EGFP protein. Immunoblot analysis of
215 nuclear extracts revealed that cells expressing WT MgdE exhibited the lower levels of
216 H3K4me3 than EGFP or $D^{244}A/H^{247}A$ double mutant (Figure 5D). Taken together, these data
217 indicate that the residues D^{244} and H^{247} are essential for the MgdE-WDR5 interaction, which

218 enables MgdE to attenuate H3K4me3 deposition in the host nuclei by subverting COMPASS
219 complex function, a mechanism critical for bacterial survival and immune evasion.

220 **MgdE suppresses host inflammatory responses probably by inhibition of COMPASS**
221 **complex-mediated H3K4 methylation**

222 As H3K4me3, a hallmark of transcriptionally active promoters, facilitates transcriptional
223 machinery assembly and RNA polymerase II recruitment (Wang et al., 2023), we further
224 investigated the transcriptional consequences of MgdE-mediated H3K4me3 suppression via
225 its interaction with the COMPASS complex. To assess the genome-wide effects of MgdE on
226 host gene expression, we performed RNA-seq profiling of THP-1 macrophages infected with
227 either WT BCG or ΔMgdE strains. Transcriptomic analysis at 24 h post-infection revealed that
228 271 genes showed significant differential expression in the cells infected with ΔMgdE strain
229 compared to that in the cells infected with WT BCG strain, with 222 genes being
230 transcriptionally upregulated in the absence of MgdE (Figure 6A). Gene ontology (GO)
231 enrichment analysis indicated that these upregulated genes were primarily associated with
232 biological processes involved in immune responses, with a notable enrichment in "Positive
233 regulation of cytokine production (GO: 0001819)", a critical pathway for amplifying
234 inflammatory signaling (Figure 6B). Furthermore, the Kyoto encyclopedia of genes and
235 genomes (KEGG) pathway enrichment analysis highlighted a significant activation of the
236 "Cytokine–cytokine receptor interaction (hsa04060)" and "JAK–STAT signaling pathway
237 (hsa04630)" in THP-1 cells infected with the ΔMgdE strain (Figure 6C, Figure S5A). Heatmap
238 analysis further confirmed the significant upregulation of inflammation-associated transcripts
239 in ΔMgdE-infected cells, including inflammatory cytokines (*IL6*, *IL7*, *IL10*, *IL12B*) and colony-

240 stimulating factors (*CSF2*–*CSF3*) (Figure 6D, Figure S56B). Protein–protein interaction
241 network analysis of the upregulated genes revealed tightly interconnected clusters within
242 inflammatory networks, particularly those orchestrated by the central inflammatory mediator
243 IL-6 (Figure S5C). To validate this result, we infected macrophages with the *M. bovis* BCG
244 strains, including WT, ΔMgdE, Comp-MgdE, and Comp-MgdE$^{\Delta NLS1\text{-}2}$, under identical
245 conditions for 24 h and examined the expression of relevant inflammatory factors. Compared
246 to cells infected with the WT and Comp-MgdE strains, those infected with the ΔMgdE and
247 Comp-MgdE$^{\Delta NLS1\text{-}2}$ strains exhibited significantly increased expression levels of inflammatory
248 factors (*IL1B*, *IL6*, *IL10*) (Figure 6E–G). Collectively, these results demonstrate that MgdE
249 effectively inhibits the production of inflammatory factors during BCG infection and highlights
250 the critical role of its NLSs in this process. Through its interaction with the COMPASS complex,
251 MgdE suppresses H3K4me3 levels, thereby attenuating the transcriptional activation of
252 inflammation-related genes.

253 **Nuclear localization of MgdE is essential for mycobacterial survival in mice**

254 Our experimental data demonstrated that MgdE enhances bacterial survival in macrophages.
255 To further investigate the *in vivo* functional significance of MgdE in host–pathogen interplay,
256 we infected C57BL/6 mice with different *M. bovis* BCG strains, including WT, ΔMgdE, Comp-
257 MgdE, and Comp-MgdE$^{\Delta NLS1\text{-}2}$, and comprehensively evaluated bacterial survival, pulmonary
258 inflammation, and cytokine dynamics. Mice infected with ΔMgdE exhibited a significantly
259 reduced lung bacterial burden compared to those infected with WT or Comp-MgdE strains.
260 Moreover, mice infected with Comp-MgdE$^{\Delta NLS1\text{-}2}$ exhibited a significantly lower pulmonary
261 bacterial load than those infected with Comp-MgdE (Figure 7A). These findings collectively

262 establish that MgdE is essential for optimal bacterial survival during infection, with the NLS
263 being critical for its full functionality. Furthermore, histopathological assessment of the lung
264 tissues corroborated these observations. Hematoxylin–eosin (H&E) staining revealed more
265 pronounced inflammatory pathology in the lungs of mice infected with WT or Comp-MgdE
266 strain compared to those infected with ΔMgdE or Comp-MgdE$^{\Delta NLS1\text{-}2}$ (Figure 7B), underscoring
267 the necessity of MgdE and its NLSs in sustaining inflammation during infection. To further
268 investigate the systemic immune modulation mediated by MgdE, we quantified splenic
269 bacterial colonization and the inflammatory cytokine profiles. Consistent with the attenuated
270 bacterial survival observed in the lungs, mice infected with ΔMgdE and Comp-MgdE$^{\Delta NLS1\text{-}2}$
271 exhibited a significantly reduced splenic bacterial load compared to those infected with WT or
272 Comp-MgdE (Figure S6). Despite diminished bacterial dissemination, infections with ΔMgdE
273 and Comp-MgdE$^{\Delta NLS1\text{-}2}$ strains triggered elevated expression of inflammatory cytokines (*Il6,*
274 *Il1b*) relative to infection with the WT and Comp-MgdE strains (Figure 7C and D). Collectively,
275 these findings indicate that MgdE orchestrates mycobacterial survival within host tissues by
276 suppressing inflammatory responses to evade pathogen clearance, with the NLS playing a
277 pivotal role in mediating these host–pathogen interactions.

278 **DISCUSSION**

279 **MgdE functions as a critical nucleomodulin that contributes to mycobacterial**
280 **pathogenesis.** Its evolutionary conservation across mycobacterial species, coupled with
281 nuclear translocation via dual N-terminal and C-terminal NLSs, supports its classification as a
282 nucleomodulin. Previous investigations have described MgdE as a secreted effector protein
283 (Penn et al., 2018), and our experimental results independently confirm its secretion (Figure

284 S2A). Furthermore, our findings demonstrate that MgdE's nuclear localization plays a critical
285 role during infection. Disruption of MgdE expression or its NLS motifs significantly attenuated
286 *M. bovis* BCG viability within macrophages (Figure 3A and B) and reduced bacterial burden in
287 mice (Figure 7A, Figure S6), supporting the notion that nuclear targeting contributes to
288 bacterial virulence. This phenotype aligns with transcriptomic data showing upregulation of
289 MgdE during *M. tuberculosis* infection of alveolar macrophages (Pisu et al., 2020). In parallel,
290 Yang et al. (2019) characterized MgdE as a lipase involved in intracellular lipid metabolism
291 and showed that its transposon mutant exhibited impaired intracellular growth in THP-1 cells
292 and PBMC-derived macrophages, as well as a moderately reduced bacterial load in
293 C3HeB/FeJ mice at later stages of infection. These findings align with our data and highlight
294 the multifaceted role of MgdE in both metabolic adaptation and host-cell interaction.
295 Together, these findings suggest a functional duality in which MgdE contributes to both
296 metabolic adaptation and host nuclear modulation. By coupling enzymatic activity with nuclear
297 targeting, MgdE may enable Mtb to balance metabolic needs and immune evasion.

298 **MgdE directly subverts the COMPASS complex to reprogram host epigenetics.** To our
299 knowledge, MgdE is the first identified bacterial effector that directly targets the COMPASS
300 complex, a central regulator of H3K4 methylation. Nuclear-localized MgdE specifically
301 interacts with the core COMPASS subunits ASH2L and WDR5, disrupting H3K4me3
302 deposition through structural interference (Guarnaccia et al., 2021; Hsu et al., 2018; Xue et
303 al., 2019). The COMPASS complex facilitates H3K4 methylation through a conserved
304 assembly mechanism involving multiple core subunits. WDR5, a central scaffolding
305 component, interacts with RbBP5 and ASH2L to promote complex assembly and enzymatic

306 activity (Qu et al., 2018; Wysocka et al., 2005). It also recognizes the WIN motif of
307 methyltransferases such as MLL1, thereby anchoring them to the complex and stabilizing the
308 ASH2L–RbBP5 dimer (Hsu et al., 2018). ASH2L further contributes to COMPASS activation
309 by interacting with both RbBP5 and DPY30 and by stabilizing the SET domain, which is
310 essential for efficient substrate recognition and catalysis (Qu et al., 2018; Park et al., 2019).
311 Our work shows that MgdE interacts with both WDR5 and ASH2L and inhibits the
312 methyltransferase activity of the COMPASS complex (Figure 4A-C, Figure 5D). Site-directed
313 mutagenesis revealed that residues D^{224} and H^{247} of MgdE are critical for WDR5 binding, as
314 the double mutant MgdE-D^{224}A/H^{247}A fails to interact with WDR5 and shows diminished
315 suppression of H3K4me3 levels (Figure 5D).

316 Moreover, MgdE accumulates in the nucleus (Figure 1C, Figure 2C, Figure 5C, Figure S2B),
317 reminiscent of *L. monocytogenes* InlP, which modulates nuclear speckles to inhibit apoptosis
318 (Pourpre et al., 2022). This interaction silences the expression of antimicrobial effector genes,
319 thereby facilitating immune evasion. Similar to *L. pneumophila* RomA, which methylates
320 H3K14 to repress innate immune responses (Schator et al., 2023; Rolando et al., 2013), or
321 Mtb Rv2067c, a structural mimic of host DOT1L that catalyzes non-nucleosomal H3K79
322 trimethylation to subvert pro-inflammatory signaling (Singh et al., 2023), MgdE exemplifies a
323 broader pathogen strategy of hijacking the host histone methylation machinery.

324 **MgdE-mediated epigenetic silencing suppresses pro-inflammatory responses.**
325 Transcriptome analysis showed that the *mgdE*-deleted BCG strain induced hyperactivation of
326 “Cytokine–cytokine receptor interaction (hsa04060)” and “JAK–STAT signaling pathway
327 (hsa04630)” (Figure 6C), along with significantly elevated production of inflammatory

328 cytokines, including *IL6* and *IL1B*, in THP-1 macrophages compared to the WT BCG strain
329 (Figure 3C and D, Figure 6E and F). This profile is consistent with the functional restoration of
330 the COMPASS complex (Wang et al., 2025; Yu et al., 2017). These findings support the
331 hypothesis that MgdE suppresses host inflammatory responses by disrupting COMPASS-
332 mediated H3K4me3 deposition at active promoters. H3K4me3 is a well-established histone
333 mark associated with transcriptional activation, in part through the recruitment of PHD domain-
334 containing reader proteins (Hyun et al., 2017). For instance, SET1-dependent deposition of
335 H3K4me3 at NF-κB target promoters facilitates the activation of inflammatory gene expression
336 (Bhattacharya et al., 2023). In addition, WDR5 has been implicated in upregulating
337 immunosuppressive cytokines, including IL6 and TGFβ (Deng et al., 2024). In transfected
338 HEK293T cells, WT MgdE significantly reduced global H3K4me3 levels, whereas the
339 catalytically inactive $D^{224}A/H^{247}A$ mutant failed to do so (Figure 5D), supporting the notion that
340 MgdE-mediated suppression of H3K4me3 depends on its ability to interact with WDR5.
341 Furthermore, during infection, the MgdE-deleted BCG strain markedly activated the
342 expression of inflammatory factors compared to the WT BCG strain (Figure 6E–G). These
343 results suggest that MgdE attenuates the expression of inflammatory mediators such as *IL6*
344 and *IL1B* by reducing host H3K4me3 levels during Mycobacterium infection. This mechanism
345 is similar to those observed in other pathogens, such as spirochete-derived factors that
346 suppress inflammation by reducing H3K4me3 levels at the *TNFα* and *IL6* promoters (Chauhan
347 et al., 2015).

348 In summary, our study identified MgdE as a critical mycobacterial nucleomodulin and
349 uncovered a novel paradigm of pathogen-mediated epigenetic regulation through the “MgdE–

350 COMPASS complex–H3K4me3–cytokine axis (Figure 7E). Mechanistically, MgdE might
351 destabilize the COMPASS assembly via the interaction with ASH2L or WDR5, resulting in
352 reduced H3K4me3 levels at the promoters of pro-inflammatory genes. This epigenetic
353 suppression downregulates cytokine transcription (e.g., *IL6 and IL1B*) and enhances bacterial
354 survival in macrophages and in mice. Our findings reveal the COMPASS complex as a
355 previously unrecognized target of bacterial effectors and offers mechanistic insights into
356 immune evasion and host–pathogen epigenetic interplay.

357 **MATERIALS AND METHODS**

358 **Bacterial strains and culture conditions**

359 The bacterial strains used in this study are detailed in Table S5. *Escherichia coli* DH5α was
360 cultured in Luria-Bertani medium under standard conditions. *Mycobacterium bovis BCG*
361 strains were grown in Middlebrook 7H9 broth (BD Biosciences), containing 1× OADC (oleic
362 acid, albumin, dextrose, catalase), 0.05% Tween-80, and 2% glycerol. Antibiotics were added
363 as required at the following final concentrations: 50 μg/mL hygromycin (for mycobacteria) and
364 50 μg/mL kanamycin (for both mycobacteria and *E. coli*). The Y2H Gold yeast strain (Takara
365 Bio) was maintained in YPDA (yeast extract, peptone, dextrose, and adenine sulfate) medium.
366 Transformants were selected on SD/-Trp medium, which lacks tryptophan, to select for
367 plasmid uptake. Protein-protein interactions were assessed in SD/-Trp/-Leu (lacking
368 tryptophan and leucine) and SD/-Trp/-Leu/-Ade/-His (lacking tryptophan, leucine, adenine,
369 and histidine) media, with growth on higher stringency media indicating positive interactions.

370 **Cell culture**

371 THP-1 cells were cultured in Roswell Park memorial institute 1640 (RPMI 1640) medium

372 supplemented with 10% (v/v) heat-inactivated fetal bovine serum (FBS), 1 mM sodium
373 pyruvate, 2 mM L-glutamine, 10 mM HEPES buffer (pH 7.2–7.5), and 50 μM 2-
374 mercaptoethanol. For differentiation into macrophages, THP-1 cells were treated with 200 nM
375 phorbol 12-myristate 13-acetate (PMA) for 48 h to allow complete differentiation prior to their
376 use in experiments.
377 HEK293T and RAW264.7 monocytes were cultured in Dulbecco's modified Eagle's medium
378 (DMEM) supplemented with 10% FBS and 50 μg/mL penicillin-streptomycin. All cells were
379 maintained at 37 °C in a humidified atmosphere with 5% CO_2.

380 **Pan-genomic nucleomodulin screening**

381 To systematically identify evolutionarily conserved nucleomodulins in pathogenic
382 mycobacteria, a pan-genomic comparative analysis was performed across four
383 phylogenetically representative mycobacterium strains: *Mycobacterium tuberculosis* H37Rv
384 (NCBI RefSeq assembly GCF_000195955.2), *Mycobacterium tuberculosis* H37Ra (NCBI
385 RefSeq assembly GCF_001938725.1), *Mycobacterium bovis* BCG (NCBI RefSeq assembly
386 GCF_000009445.1), *Mycobacterium marinum* (NCBI RefSeq assembly GCF_000018345.1),
387 and *Mycobacterium avium* subsp (NCBI RefSeq assembly GCF_009741445.1). Complete
388 genome sequences and annotations were obtained from NCBI RefSeq with strict inclusion
389 criteria requiring "Complete Genome" status and fewer than 50 contigs to ensure the assembly
390 integrity. Plasmid sequences, as well as low-complexity and repetitive regions, were filtered
391 using the NCBI Genome Data Viewer toolkit. Genome quality control was rigorously conducted
392 using CheckM v1.2.2 with a *Mycobacteriaceae*-specific marker set (including essential
393 housekeeping genes such as *dnaA* and *rpoB*), confirming that all the selected genomes

394 exhibited >99% completeness and <1% contamination.

395 Ortholog clustering of protein–coding sequences (CDS) was executed through OrthoFinder
396 v2.5.4, employing Diamond alignment in ultra-sensitive mode (--ultra-sensitive), an E-value
397 cutoff of ≤1e-5 (--blastp_evalue 1e-5), and a minimum sequence identity threshold of ≥50% (-
398 -min_percent_identity 50). The Markov cluster algorithm (MCL) was applied with an inflation
399 parameter of 1.5 (--mcl_inflation 1.5) to define orthologous groups, balancing sensitivity, and
400 specificity. Core orthologs were identified as clusters present in all four strains, with additional
401 filtering to retain only single-copy genes in ≥90% of the strains, minimizing paralog-related
402 artifacts.

403 Functional annotation of the core genes was conducted using InterProScan v5.62, which
404 integrates domain predictions from the Pfam, TIGRFAM, and SUPERFAMILY databases. To
405 prioritize candidate nucleomodulins, a sequential screening pipeline was applied, beginning
406 with the prediction of classical secretory proteins using SignalP v5.0 (D-score ≥0.5), followed
407 by the identification of non-classically secreted proteins via SecretomeP v2.0 (NN score ≥0.9),
408 and culminating in NLS detection using cNLS Mapper (NLS score ≥2.0), which predicts both
409 monopartite and bipartite NLSs. This integrated strategy enabled the systematic identification
410 of conserved candidates that exhibit both secretory potential and nuclear targeting capacity.

411 **Immunoblot analysis of MgdE secretion**

412 The procedure for immunoblot analysis of MgdE secretion was adapted from Zhang et al.
413 (2022) with minor modifications. *M. bovis* BCG strains expressing C-terminally Flag-tagged
414 MgdE were cultured in Middlebrook 7H9 broth supplemented with 0.5% glycerol, 0.02%

415 Tyloxapol, and 50 μg/mL kanamycin. Cultures were incubated at 37 °C with gentle agitation
416 (80 rpm) until reaching an OD_{600} of ~0.6. Cells were harvested by centrifugation at 4,000 × *g*
417 for 15 min at 4 °C. The culture supernatants were filtered through 0.22 μm PES membranes
418 (Millipore) to remove residual bacteria and subsequently concentrated ~100-fold using Amicon
419 Ultra-15 centrifugal filters with a 10 kDa molecular weight cutoff (Millipore). The resulting
420 culture filtrates were used for detection of secreted MgdE. Bacterial pellets were washed twice
421 with PBS and resuspended in lysis buffer containing 50 mM Tris-HCl (pH 7.5), 150 mM NaCl,
422 1 mM PMSF, and 1× protease inhibitor cocktail. Cells were lysed by sonication on ice, and the
423 lysates were cleared by centrifugation at 10,000 × *g* for 15 min at 4 °C to obtain whole-cell
424 lysates. Whole-cell lysates and concentrated culture filtrates were resolved on 10% SDS–
425 PAGE gels and transferred to PVDF membranes (Millipore). Membranes were blocked with
426 5% skimmed milk powder in TBST (Tris-buffered saline containing 0.1% Tween-20) for 1 h at
427 room temperature and then incubated overnight at 4 °C with a monoclonal anti-Flag antibody.
428 After washing, membranes were incubated with HRP-conjugated secondary antibodies for 1 h
429 at room temperature. Immunoreactive bands were visualized using enhanced
430 chemiluminescence (ECL) substrate and imaged with a ChemiDoc MP imaging system (Bio-
431 Rad).

432 **Phylogenetic and sequence analysis**

433 To investigate the evolutionary conservation and sequence features of MgdE homologs,
434 phylogenetic reconstruction was performed using MEGA 12.0 with a neighbor-joining
435 algorithm. The parameters included pairwise deletion for gap treatment, a Poisson substitution
436 model (selected for its suitability in analyzing closely related bacterial sequences), and 1,000

437 bootstrap replicates to assess node support. Nodes with ≥50% bootstrap values were retained,
438 and no additional pruning was performed.
439 The analysis incorporated MgdE homologs from 12 Mycobacterium strains spanning clinical,
440 environmental, and attenuated lineages. These included Rv1075c (*M. tuberculosis* H37Rv),
441 BCG_1133c (*M. bovis* BCG), MRA_1085 (*M. tuberculosis* H37Ra), MAF_10880 (*M.*
442 *africanum*), MT1105 (*M. tuberculosis* CDC1551), TBMG_02912 (*M. tuberculosis* GM041182),
443 MSHI_02760 (*M. shinjukuense*), MMAR_4392 (*M. marinum*), MULP_04607 (*M. lupini*),
444 MAV_1199 (*M. avium*), MMAN_54310 (*M. manitobense*), and MIP_01781 (*M. intracellulare*).
445 Genomic sequences were retrieved from the NCBI RefSeq database, filtered for
446 completeness, and aligned using Clustal Omega v1.2.4 with default parameters (gap opening
447 penalty = 10, gap extension = 0.2, and iterative refinement enabled). Sequence conservation
448 was visualized using ESPript 3.0, highlighting residues with ≥90% identity across all homologs
449 in red.

450 **Computational prediction of sequence and structural features**

451 AlphaFold v2.2.0 was used to predict the interaction between MgdE and COMPASS complex
452 subunits, following the methodology established in a previous study (Gómez Borrego et al.,
453 2024). The specific parameters used for the prediction were as follows: model_preset =
454 multimer; db_preset = full_dbs. A FASTA file containing the sequences of both MgdE and
455 COMPASS complex subunit proteins was input into the AlphaFold software. The resulting
456 models were evaluated and ranked based on the AF-score, which is a linear combination of
457 the interface score (ipTM) and the predicted TM-score (pTM). The top-ranked model (rank 1)
458 was selected for further analysis.

459 **Cell transfection and confocal microscopy**

460 HEK293T cells were seeded at 70% confluency in poly-L-lysine-coated 35-mm glass-bottom
461 dishes and maintained in DMEM supplemented with 10% FBS at 37 °C under 5% CO_2.
462 Transfection was performed using the Hieff Trans™ Liposomal Transfection Reagent (Yeasen)
463 according to the manufacturer's protocol. Briefly, 0.5 μg of DNA and 1.5 μL of transfection
464 reagent were mixed with 50 μL of Opti-MEM and incubated for 20 min at room temperature.
465 The mixture was added dropwise to each chamber of 35-mm six-chamber glass-bottom dishes
466 containing cells at 40–60% confluency.

467 At 4–48 h post-transfection, the cells were washed with PBS, fixed in 4% paraformaldehyde
468 for 15 min, and permeabilized with 0.1% Triton X-100 for 10 min. Nuclei were counterstained
469 with 1 μg/mL DAPI for 10 min. Confocal imaging was performed using an Olympus FV1000
470 Confocal Laser Scanning Microscope equipped with a 100×/1.40 NA oil immersion objective.
471 EGFP and DAPI signals were detected with 488 nm and 405 nm lasers, respectively. Spectral
472 unmixing was applied using the Olympus FV10-ASW software (v4.2) to minimize signal cross-
473 talk, and Z-stacks were acquired in sequential mode by applying a step size of 0.5 μm across
474 all samples to ensure comparability.

475 **Cell fractionation and Immunoblotting**

476 During infection, THP-1 cells were differentiated with 200 ng/mL PMA for 48 hours, followed
477 by infection with BCG/MgdE-Flag, BCG/MgdE$^{\Delta NLS1}$-Flag, BCG/MgdE$^{\Delta NLS2}$-Flag, or
478 BCG/MgdE$^{\Delta NLS1-2}$ -Flag strains at a multiplicity of infection (MOI) of 50 for 24 hours. Cell
479 fractionation was performed with minor modifications based on a previously described method
480 (Wang J et al., 2017). Briefly, cells were lysed in a hypotonic buffer containing 10 mM HEPES

481 (pH 7.9), 1.5 mM $MgCl_2$, 10 mM KCl, 0.34 M sucrose, 10% glycerol, and 0.02% Tyloxapol,
482 supplemented with 1% protease inhibitor cocktail, and incubated for 10 minutes at 4 °C. The
483 lysates were then centrifuged at 1300 × *g* for 10 minutes. The pellet from uninfected THP-1
484 cells was collected as the nuclear fraction. For infected THP-1 cells, the pellet was
485 resuspended in PBS containing 0.1% SDS and centrifuged at 2500 × *g* for 15 minutes at 4 °C.
486 The resulting supernatant was collected as the nuclear fraction.
487 During transfection, HEK293T cells were cultured in DMEM supplemented with 10% FBS at
488 37 °C in a 5% CO_2 incubator. Transfection was performed as described in the "Cell transfection
489 and confocal microscopy" section. At 36 hours post-transfection, nuclear and cytoplasmic
490 protein fractionation was conducted using the Nuclear and Cytoplasmic Protein Extraction Kit
491 (Beyotime) with minor modifications. Cells were washed with PBS, detached using a cell
492 scraper, and pelleted by centrifugation at 2000 × *g* for 5 minutes. After removing the
493 supernatant, 150 μL of Cytoplasmic Extraction Reagent A (with PMSF) was added to ~20 μL
494 of packed cells, vortexed for 5 seconds, and incubated on ice for 15 minutes. Then, 10 μL of
495 Reagent B was added, followed by vortexing and ice incubation. The mixture was centrifuged
496 at 12,000 × *g* for 5 minutes at 4 °C, and the supernatant was collected as the cytoplasmic
497 fraction. The pellet was resuspended in 50 μL of Nuclear Extraction Reagent (with PMSF),
498 vortexed intermittently over 30 minutes on ice, and centrifuged at 12,000 × *g* for 10 minutes
499 at 4 °C. The resulting supernatant was collected as the nuclear protein fraction.

500 Protein concentrations were quantified using the BCA assay (Thermo Fisher Scientific). Equal
501 amounts of protein (20–40 μg) were resolved by sodium dodecylsulfate polyacrylamide gel
502 electrophoresis (SDS–PAGE) and transferred onto PVDF membranes (Millipore). The

503 membranes were blocked for 1 h at room temperature with 5% non-fat milk in TBST (25 mM
504 Tris, 150 mM NaCl, 2 mM KCl, and 0.2% Tween-20, pH 7.4) and incubated overnight at 4 °C
505 with primary antibodies. After three washes with TBST (6 min each), the membranes were
506 incubated with HRP-conjugated secondary antibodies at room temperature for 1 h. Following
507 three additional TBST washes, protein signals were detected using an enhanced
508 chemiluminescence (ECL) substrate and imaged on a ChemiDoc MP system (Bio-Rad). The
509 antibody information is listed in Table S4.

510 **Co-IP assays**

511 The Co-IP assays were performed to analyze protein-protein interactions. HEK293T cells were
512 washed twice with ice-cold PBS and lysed in lysis buffer (50 mM Tris-HCl, pH 7.4, 150 mM
513 NaCl, 1% NP-40) supplemented with 1.5% protease inhibitor cocktail (Boster) for 30 min on
514 ice. Crude lysates were centrifuged at 12,000 ×*g* for 15 min at 4 °C to remove the debris. For
515 immunoprecipitation, 1 mg of total protein was incubated with 5 μg of primary antibody
516 overnight at 4 °C with gentle agitation. Protein A/G magnetic beads (MedChemExpress) were
517 added to the antibody-protein complexes and incubated for 6 h at 4 °C. The beads were
518 washed three times with PBS-T buffer (PBS containing 0.5% Tween-20) to remove nonspecific
519 interactions. Proteins were eluted by boiling the beads in 1× SDS sample buffer at 95 °C for 5
520 min. The eluted proteins were resolved by SDS-PAGE and analyzed by immunoblotting.
521 Antibody information is listed in Table S4.

522 **Y2H assay**

523 The Yeast Two-Hybrid System (Clontech) was used to assay protein-protein interactions

524 between MgdE (WT and mutants) and subunits of the COMPASS complex (ASH2L, WDR5,
525 RbBP5, and DPY30). Full-length cDNAs encoding WT MgdE and its mutants (see Table S6)
526 were cloned into the bait vector pGBKT7, whereas genes encoding the COMPASS subunits
527 were cloned into the prey vector pGADT7. The yeast strain Y2H Gold was co-transformed with
528 bait and prey plasmids using the lithium acetate/polyethylene glycol method, and the
529 transformed colonies were initially selected on SD agar plates lacking leucine and tryptophan
530 (-Leu/-Trp) to confirm plasmid retention. For interaction screening, colonies were replica-
531 plated onto selective SD agar plates lacking leucine, tryptophan, adenine, and histidine (-Leu/-
532 Trp/-Ade/-His) and supplemented with 200 ng/μL aureobasidin A (AbA, Sigma-Aldrich). The
533 plates were incubated at 30 °C, and colony growth was monitored daily, with final assessments
534 performed after 5 days of incubation. Interaction strength was qualitatively assessed by
535 comparing colony density and growth rates with those of the controls. The positive controls
536 included the co-transformation of pGBKT7-p53 with pGADT7-T, which produced robust growth
537 on -Leu/-Trp/-Ade/-His plates. Negative controls included co-transformation of pGBKT7-Lam
538 (human lamin C, a non-interacting bait) with pGADT7-T, as well as individual transformations
539 with empty pGBKT7 or pGADT7 vectors to assess the background growth. The yeast strains
540 used in this study are listed in Table S5.

541 **RNA-seq analysis**

542 THP-1 cells were seeded at a density of 1 × 10^6 cells/well in 6-well plates and differentiated
543 into macrophages by treatment with 200 nM PMA for 48 h. Following differentiation, the cells
544 were washed with PBS and infected with *M. bovis* BCG WT or ΔMgdE strains at a MOI of 10:1.
545 Following 24 h of infection, total RNA was extracted using TRIzol® reagent (Thermo Fisher

546 Scientific) according to the manufacturer's instructions. High-quality reads were then mapped
547 to the human reference genome (GRCh38) using HISAT2 (v2.2.1). FeatureCounts (v2.0.3)
548 was used to quantify transcript abundance, and differential gene expression analysis was
549 conducted using DESeq2 (v1.38.3) in R. Genes with an adjusted *P*-value <0.05 and an
550 absolute log_2-foldchange ≥1 was considered significantly differentially expressed. RNA-seq
551 data were visualized using GraphPad Prism 8.0, and volcano plots, heatmaps, and other
552 visualizations were generated to summarize the results.

553 **qRT-PCR assay**

554 THP-1 cells were infected with the *M. bovis* BCG strain and harvested 24 h post-infection for
555 RNA isolation. Total RNA was extracted using 1 mL of TRIzol® reagent (Aidlab) according to
556 the manufacturer's instructions. To remove genomic DNA contamination, the RNA samples
557 were treated with DNase I (Thermo Fisher Scientific) for 30 min at 37 °C, followed by heat
558 inactivation at 65 °C for 10 min. RNA concentration and purity were assessed using a
559 NanoDrop 2000 spectrophotometer (Thermo Fisher Scientific). For cDNA synthesis, 1 μg of
560 total RNA was reverse transcribed using the HiScript® III cDNA Reverse Transcription Kit
561 (Vazyme) with random hexamers, according to the manufacturer's protocol. qRT-PCR was
562 performed using ChamQ SYBR® Green RT-PCR Master Mix (Vazyme). The relative mRNA
563 expression of different genes was calculated by comparing their cycle threshold (Ct) values to
564 that of a control gene *hprt* using the $2^{-\Delta\Delta Ct}$ method. Real-time qRT-PCR experiments were
565 performed in triplicate, with at least three independent biological replicates and two technical
566 replicates per condition. Primer sequences used for qRT-PCR are listed in Table S7.

567 **CFU assay**

568 For bacterial preparation, mid-log phase cultures (OD_{600} = 0.8) of *M. bovis* BCG were washed
569 with PBS and resuspended in fresh medium. THP-1 cells were seeded at a density of 5×10^5
570 cells/well in 24-well plates and subsequently infected at a MOI of 10:1. Following 4 h of
571 infection, extracellular bacteria were eliminated by treatment with penicillin-streptomycin (100
572 μg/mL) for 2 h. The cells were then washed three times with PBS and maintained in an
573 antibiotic-free medium until harvest. For bacterial recovery, the macrophages were lysed with
574 0.25% SDS for 10 min at room temperature, followed by serial dilution of the lysates in PBS.
575 Aliquots (100 μL) of each dilution were plated on Middlebrook 7H10 agar supplemented with
576 10% OADC and kanamycin (50 μg/mL). Plates were incubated at 37 °C for 14 days, and CFUs
577 were calculated by applying dilution factors to the colony counts. *M. bovis* BCG strains used
578 in this study are listed in Table S5.

579 **Animal experiments**

580 Specific pathogen-free (SPF) female C57BL/6 mice (6–8 weeks old) were obtained from
581 Chang-sheng Bio (Liaoning, China). All animals were housed under SPF conditions under
582 controlled temperature, humidity, and a 12-hour light/dark cycle, with free access to food and
583 water.

584 Mice were infected as described previously with slight modifications (Chen et al., 2022). Mid-
585 log phase *M. bovis* BCG cultures were washed twice in PBS containing 0.05% Tween 80 and
586 sonicated to disrupt clumps. Female C57BL/6 mice (6–8 weeks old, 16–18g) were
587 anesthetized using isoflurane and intranasally administered 1×10^7 CFUs of *M. bovis* BCG in
588 40 μL of PBS. At 2 days post-infection, the bacterial load in the lungs of six mice was assessed
589 to confirm the inoculation dose. The lungs were homogenized in 1 mL of PBS using a tissue

590 homogenizer, and serial dilutions of the homogenates were plated onto Middlebrook 7H10
591 agar with 10% OADC. The plates were then incubated at 37 °C with 5% CO_2 for 14 d prior to
592 colony counting.

593 **Histological analysis**

594 Lung tissues from *M. bovis* BCG-infected mice were fixed in 4% phosphate-buffered formalin
595 at room temperature for 24 h and embedded in paraffin wax. Paraffin-embedded tissue
596 samples were sectioned into 2–3 μm thick slices using a microtome. The sections were
597 deparaffinized, rehydrated with graded ethanol, and stained with hematoxylin and eosin (H&E).
598 Stained slides were visualized using an Olympus BX53 light microscope, and CaseViewer
599 version 2.0 (3DHISTECH) was used to view and annotate the scanned slides.

600 **Ethics approval**

601 All animal experiments were conducted in accordance with the protocols approved by the
602 Animal Ethics Committee of the Huazhong Agricultural University.

603 **Statistical analyses**

604 Data are presented as mean ± standard deviation (SD). For comparisons between the two
605 groups, statistical significance was determined using two-tailed unpaired Student's *t*-tests after
606 confirming normality. Statistical significance was set at $P < 0.05$. Significance levels are
607 denoted in the figures as follows: $P > 0.05$ (ns, not significant), $P < 0.05$ (*), $P < 0.01$ (**), and
608 $P < 0.001$ (***). All statistical analyses were performed using GraphPad Prism (version 8.0).
609 Data were collected from at least three independent biological replicates, each with two or
610 more technical replicates.

ACKNOWLEDGMENTS

This work was supported by the National Key Research and Development Program of China (#2021YFD1800403), Fundamental Research Funds for the Central Universities (#2662023DKQD001), Talent Start-up Funds of Huazhong Agricultural University (#11042310008), National Natural Science Foundation of China (#32473123), China Agriculture Research System of MOF and MARA (#CARS-37).

AUTHOR CONTRIBUTIONS

Conceptualization: L. C., A. G., and L. Z.; Methodology: L. C.; Validation: L. C., B. D., and Q. J.; Formal analysis: L. C., Y. W.; Investigation: L. C., B. D., P. C., Q. J., Y. W., and L. L.; Resources: A. G., L. Z., and Y. C.; Data curation: L. C., Q. J., Y. W., and L. L.; Writing - original draft: L. C., L. Z., and A. G.; Writing - review & editing: L. C., L. Z., and A. G.; Visualization: L. C., Q. J., Y. C., C. H., L. Z., and A. G.; Supervision: A. G., L. Z., Y. C., and C. H.; Project administration: A. G., L. Z., Y. C., and C. H.; Funding acquisition: A. G., L. Z., and Y. C.

DISCLOSURE AND COMPETING INTEREST STATEMENT

The authors declare no competing interests.

REFERENCES

Bates TA, Trank-Greene M, Nguyenla X, Anastas A, Gurmessa SK, Merutka IR, Dixon SD, Shumate A, Groncki AR, Parson MAH (2024) **ESAT-6 undergoes self-association at phagosomal pH and an ESAT-6-specific nanobody restricts *M. tuberculosis* growth in macrophages** *Elife* **12**:RP91930.

631 Bendtsen JD, Kiemer L, Fausbøll A, Brunak S (2005) **Non-classical protein secretion in**
632 **bacteria** *BMC Microbiol* **5**:58.

633 Bhattacharya A, Fushimi A, Wang K, Yamashita N, Morimoto Y, Ishikawa S, Daimon T, Liu T,
634 Liu S, Long MD (2023) **MUC1-C intersects chronic inflammation with epigenetic**
635 **reprogramming by regulating the set1a compass complex in cancer progression**
636 *Commun Biol* **6**:1030.

637 Bierne H, Cossart P (2012) **When bacteria target the nucleus: the emerging family of**
638 **nucleomodulins** *Cell Microbiol* **14**:622-633.

639 Bierne H, Pourpre R (2020) **Bacterial factors targeting the nucleus: the growing family of**
640 **nucleomodulins** *Toxins* (Basel) **12**:220.

641 Chai Q, Wang L, Liu CH, Ge B (2020) **New insights into the evasion of host innate**
642 **immunity by *Mycobacterium tuberculosis*** *Cell Mol Immunol* **17**:901-913.

643 Chai Q, Yu S, Zhong Y, Lu Z, Qiu C, Yu Y, Zhang X, Zhang Y, Lei Z, Qiang L (2022) **A bacterial**
644 **phospholipid phosphatase inhibits host pyroptosis by hijacking ubiquitin** *Science*
645 **378**:eabq0132.

646 Chambers KA, Scheck RA (2020) **Bacterial virulence mediated by orthogonal post-**
647 **translational modification** *Nat Chem Biol* **16**:1043-1051.

648 Chandra P, Grigsby SJ, Philips JA (2022) **Immune evasion and provocation by**
649 ***Mycobacterium tuberculosis*** *Nat Rev Microbiol* **20**:750-766.

650 Chauhan A, Quenum FZ, Abbas A, Bradley DS, Nechaev S, Singh BB, Sharma J, Mishra BB

651 (2015) **Epigenetic modulation of microglial inflammatory gene loci in helminth-induced**
652 **immune suppression: implications for immune regulation in neurocysticercosis** *ASN*
653 *Neuro* **7**:1759091415592126.

654 Chen L, Li X, Xu P, He ZG (2022) **A Novel Zinc Exporter CtpG Enhances Resistance to**
655 **Zinc Toxicity and Survival in *Mycobacterium bovis*** *Microbiol Spectr* **10**:e0145621.

656 Deng K, Liang L, Yang Y, Wu Y, Li Y, Zhang R, Tian Y, Lu C (2024) **The Wdr5-H3K4me3**
657 **epigenetic axis regulates pancreatic tumor immunogenicity and immune suppression**
658 *Int J Mol Sci* **25**:8773.

659 Denzer L, Schroten H, Schwerk C (2020) **From gene to protein-how bacterial virulence**
660 **factors manipulate host gene expression during infection** *Int J Mol Sci* **21**:3730.

661 Evans SM, Rodino KG, Adcox HE, Carlyon JA (2018) ***Orientia tsutsugamushi* uses two Ank**
662 **effectors to modulate NF-κB p65 nuclear transport and inhibit NF-κB transcriptional**
663 **activation** *PLoS Pathog* **14**:e1007023.

664 Fol M, Włodarczyk M, Druszczyńska M (2020) **Host epigenetics in intracellular pathogen**
665 **infections** *Int J Mol Sci* **21**:4573.

666 Fu M, Liang S, Wu J, Hua Y, Chen H, Zhang Z, Liu J, Li X, Zhang B, Zhao W, Wan C (2021)
667 **An *Escherichia coli* effector protein EspF may induce host DNA damage via interaction**
668 **with SMC1** *Front Microbiol* **12**:682064.

669 Gómez Borrego J, Torrent Burgas M (2024) **Structural assembly of the bacterial essential**
670 **interactome** *Elife* **13**:e94919.

671 Guarnaccia AD, Rose KL, Wang J, Zhao B, Popay TM, Wang CE, Guerrazzi K, Hill S, Woodley
672 CM, Hansen TJ (2021) **Impact of WIN site inhibitor on the WDR5 interactome** *Cell Rep*
673 **34**:108636.

674 Hammond DE, Kumar JD, Raymond L, Simpson DM, Beynon RJ, Dockray GJ, Varro A (2018)
675 **Stable isotope dynamic labeling of secretomes (SIDLS) identifies authentic secretory**
676 **proteins released by cancer and stromal cells** *Mol Cell Proteomics* **17**:1837-1849.

677 Hanford HE, Von Dwingelo J, Abu Kwaik Y (2021) **Bacterial nucleomodulins: a**
678 **coevolutionary adaptation to the eukaryotic command center** *PLoS Pathog* **17**:e1009184.

679 Hsu PL, Li H, Lau HT, Leonen C, Dhall A, Ong SE, Chatterjee C, Zheng N (2018) **Crystal**
680 **structure of the COMPASS H3K4 methyltransferase catalytic module** *Cell* **174**:1106-
681 1116.e9.

682 Hyun K, Jeon J, Park K, Kim J (2017) **Writing, erasing and reading histone lysine**
683 **methylations** *Exp Mol Med* **49**:e324.

684 Jose L, Ramachandran R, Bhagavat R, Gomez RL, Chandran A, Raghunandanan S,
685 Omkumar RV, Chandra N, Mundayoor S, Kumar RA (2016) **Hypothetical protein Rv3423.1**
686 **of *Mycobacterium tuberculosis* is a histone acetyltransferase** *FEBS J* **283**:265-281.

687 Khan AA, Khan Z (2021) **Bacterial nucleomodulins and cancer: an unresolved enigma**
688 *Transl Oncol* **14**:100922.

689 Lebreton A, Job V, Ragon M, Le Monnier A, Dessen A, Cossart P, Bierne H (2014) **Structural**
690 **basis for the inhibition of the chromatin repressor BAHD1 by the bacterial**

691 **nucleomodulin LntA** *mBio* **5**:e00775-13.

692 Park SH, Ayoub A, Lee YT, Xu J, Kim H, Zheng W, Zhang B, Sha L, An S, Zhang Y, Cianfrocco
693 MA, Su M, Dou Y, Cho US (2019) **Cryo-EM structure of the human MLL1 core complex**
694 **bound to the nucleosome** *Nat Commun* **10**:5540.

695 Penn BH, Netter Z, Johnson JR, Von Dollen J, Jang GM, Johnson T, Ohol YM, Maher C, Bell
696 SL, Geiger K (2018) **An Mtb-human protein-protein interaction map identifies a switch**
697 **between host antiviral and antibacterial responses** *Mol Cell* **71**:637-648.e5.

698 Pisu D, Huang L, Grenier JK, Russell DG (2020) **Dual RNA-Seq of Mtb-Infected**
699 **Macrophages In Vivo Reveals Ontologically Distinct Host-Pathogen Interactions** *Cell*
700 *Rep* **30**:335-350.e4.

701 Pourpre R, Lakisic G, Desgranges E, Cossart P, Pagliuso A, Bierne H (2022) **A bacterial**
702 **virulence factor interacts with the splicing factor RBM5 and stimulates formation of**
703 **nuclear RBM5 granules** *Sci Rep* **12**:21961.

704 Prokop A, Gouin E, Villiers V, Nahori MA, Vincentelli R, Duval M, Cossart P, Dussurget O (2017)
705 **OrfX, a nucleomodulin required for *Listeria monocytogenes* virulence** *mBio* **8**:e01550-
706 17.

707 Qiang L, Zhang Y, Lei Z, Lu Z, Tan S, Ge P, Chai Q, Zhao M, Zhang X, Li B (2023) **A**
708 **mycobacterial effector promotes ferroptosis-dependent pathogenicity and**
709 **dissemination** *Nat Commun* **14**:1430.

710 Qu Q, Takahashi YH, Yang Y, Hu H, Zhang Y, Brunzelle JS, Couture JF, Shilatifard A, Skiniotis

711 G (2018) **Structure and Conformational Dynamics of a COMPASS Histone H3K4**
712 **Methyltransferase Complex** *Cell* **174**:1117-1126.e12.

713 Radoshevich L, Cossart P (2018) ***Listeria monocytogenes*: towards a complete picture of**
714 **its physiology and pathogenesis** *Nat Rev Microbiol* **16**:32-46.

715 Rennoll-Bankert KE, Garcia-Garcia JC, Sinclair SH, Dumler JS (2015) **Chromatin-bound**
716 **bacterial effector ankyrin A recruits histone deacetylase 1 and modifies host gene**
717 **expression** *Cell Microbiol* **17**:1640-1652.

718 Rolando M, Sanulli S, Rusniok C, Gomez-Valero L, Bertholet C, Sahr T, Margueron R,
719 Buchrieser C (2013) ***Legionella pneumophila* effector RomA uniquely modifies host**
720 **chromatin to repress gene expression and promote intracellular bacterial replication**
721 *Cell Host Microbe* **13**:395-405.

722 Rolando M, Wah Chung IY, Xu C, Gomez-Valero L, England P, Cygler M, Buchrieser C (2023)
723 **The SET and ankyrin domains of the secreted *Legionella pneumophila* histone**
724 **methyltransferase work together to modify host chromatin** *mBio* **14**:e0165523.

725 Schator D, Mondino S, Berthelet J, Di Silvestre C, Ben Assaya M, Rusniok C, Rodrigues-Lima
726 F, Wehenkel A, Buchrieser C, Rolando M (2023) **Legionella para-effectors target chromatin**
727 **and promote bacterial replication** *Nat Commun* **14**:2154.

728 Sharma G, Upadhyay S, Srilalitha M, Nandicoori VK, Khosla S (2015) **The interaction of**
729 **mycobacterial protein Rv2966c with host chromatin is mediated through non-CpG**
730 **methylation and histone H3/H4 binding** *Nucleic Acids Res* **43**:3922-3937.

731 Singh PR, Dadireddy V, Udupa S, Kalladi SM, Shee S, Khosla S, Rajmani RS, Singh A,
732 Ramakumar S, Nagaraja V (2023) **The *Mycobacterium tuberculosis* methyltransferase**
733 **Rv2067c manipulates host epigenetic programming to promote its own survival** *Nat*
734 *Commun* **14**:8497.

735 Sun H, Kamanova J, Lara-Tejero M, Galán JE (2016) **A Family of Salmonella Type III**
736 **Secretion Effector Proteins Selectively Targets the NF-κB Signaling Pathway to**
737 **Preserve Host Homeostasis** *PLoS Pathog* **12**:e1005484.

738 Wang H, Fan Z, Shliaha PV, Miele M, Hendrickson RC, Jiang X, Helin K (2023) **H3K4me3**
739 **regulates RNA polymerase II promoter-proximal pause-release** *Nature* **615**:339-348.

740 Wang H, Helin K (2025) **Roles of H3K4 methylation in biology and disease** *Trends Cell*
741 *Biol* **35**:115-128.

742 Wang J, Ge P, Qiang L, Tian F, Zhao D, Chai Q, Zhu M, Zhou R, Meng G, Iwakura Y (2017)
743 **The mycobacterial phosphatase PtpA regulates the expression of host genes and**
744 **promotes cell proliferation** *Nat Commun* **8**:244.

745 Wysocka J, Swigut T, Milne TA, Dou Y, Zhang X, Burlingame AL, Roeder RG, Brivanlou AH,
746 Allis CD (2005) **WDR5 associates with histone H3 methylated at K4 and is essential for**
747 **H3 K4 methylation and vertebrate development** *Cell* **121**:859-72.

748 Xue H, Yao T, Cao M, Zhu G, Li Y, Yuan G, Chen Y, Lei M, Huang J (2019) **Structural basis**
749 **of nucleosome recognition and modification by MLL methyltransferases** *Nature*
750 **573**:445-449.

751 Yang D, He X, Li S, Liu J, Stabenow J, Zalduondo L, White S, Kong Y (2019) **Rv1075c of**
752 ***Mycobacterium tuberculosis* is a GDSL-Like esterase and is important for intracellular**
753 **survival** *J Infect Dis* **220**:677-686.

754 Yaseen I, Kaur P, Nandicoori VK, Khosla S (2015) **Mycobacteria modulate host epigenetic**
755 **machinery by Rv1988 methylation of a non-tail arginine of histone H3** *Nat Commun*
756 **6**:8922.

757 Yu H, Lesch BJ (2024) **Functional roles of H3K4 methylation in transcriptional regulation**
758 *Mol Cell Biol* **44**:505-515.

759 Yu L, Fang F, Dai X, Xu H, Qi X, Fang M, Xu Y (2017) **MKL1 defines the H3K4Me3 landscape**
760 **for NF-κB dependent inflammatory response** *Sci Rep* **7**:191.

761 Zhang L, Kent JE, Whitaker M, Young DC, Herrmann D, Aleshin AE, Ko YH, Cingolani G, Saad
762 JS, Moody DB, Marassi FM, Ehrt S, Niederweis M (2022) **A periplasmic cinched protein is**
763 **required for siderophore secretion and virulence of Mycobacterium tuberculosis** *Nat*
764 *Commun* **13**:2255.

765 Zhang YJ, Reddy MC, Ioerger TR, Rothchild AC, Dartois V, Schuster BM, Trauner A, Wallis D,
766 Galaviz S, Huttenhower C, Sacchettini JC, Behar SM, Rubin EJ (2013) **Tryptophan**
767 **biosynthesis protects mycobacteria from CD4 T-cell-mediated killing** *Cell* **155**:1296-308.

768 Zhao J, Liu Y, Lin F, Wang W, Yang S, Ge Y, Chen PR (2019) **Bioorthogonal engineering of**
769 **bacterial effectors for spatial-temporal modulation of cell signaling** *ACS Cent Sci* **5**:145-
770 152.

Figures

Figure legends

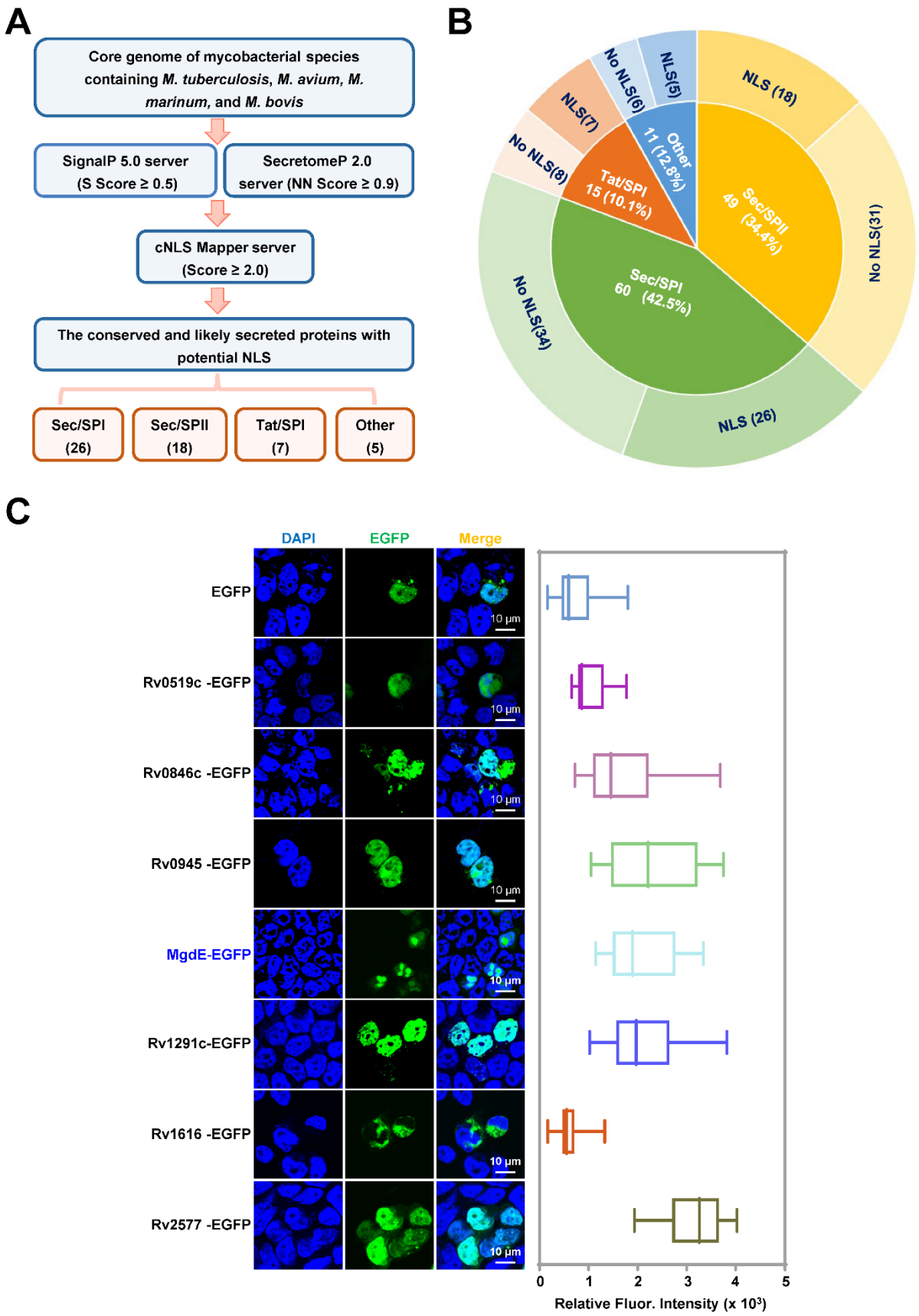

774

775 **Figure 1. Identification of conserved nucleomodulins in mycobacteria through**

776 **functional screening.**

777 (**A**) Schematic representation of the bioinformatic pipeline for identifying conserved
778 nucleomodulins in Mycobacterium species. Genomic sequences from *M. tuberculosis* H37Rv,
779 *M. tuberculosis* H37Ra, *M. avium*, *M. marinum*, and *M. bovis* BCG were analyzed. Signal
780 peptides were predicted using SignalP 5.0 (D-score ≥ 0.5), non-classical secretion signals
781 were identified using SecretomeP 2.0 (NN score ≥ 0.9), and nuclear localization signals (NLSs)
782 were predicted using cNLS Mapper (score ≥ 2.0). (**B**) Classification of conserved cellular
783 nucleomodulins. Secreted proteins were categorized based on the presence or absence of
784 predicted NLS motifs. (**C**) Subcellular localization of EGFP-tagged candidate nucleomodulins.
785 (left) Confocal microscopy images of seven Tat/SPI proteins fused to EGFP (green), nuclei
786 were stained with DAPI (blue). (right) Quantification of nuclear EGFP fluorescence intensity.
787 Scale bar, 10 μm. Data are presented as mean ± SD (n = 25 cells/group).

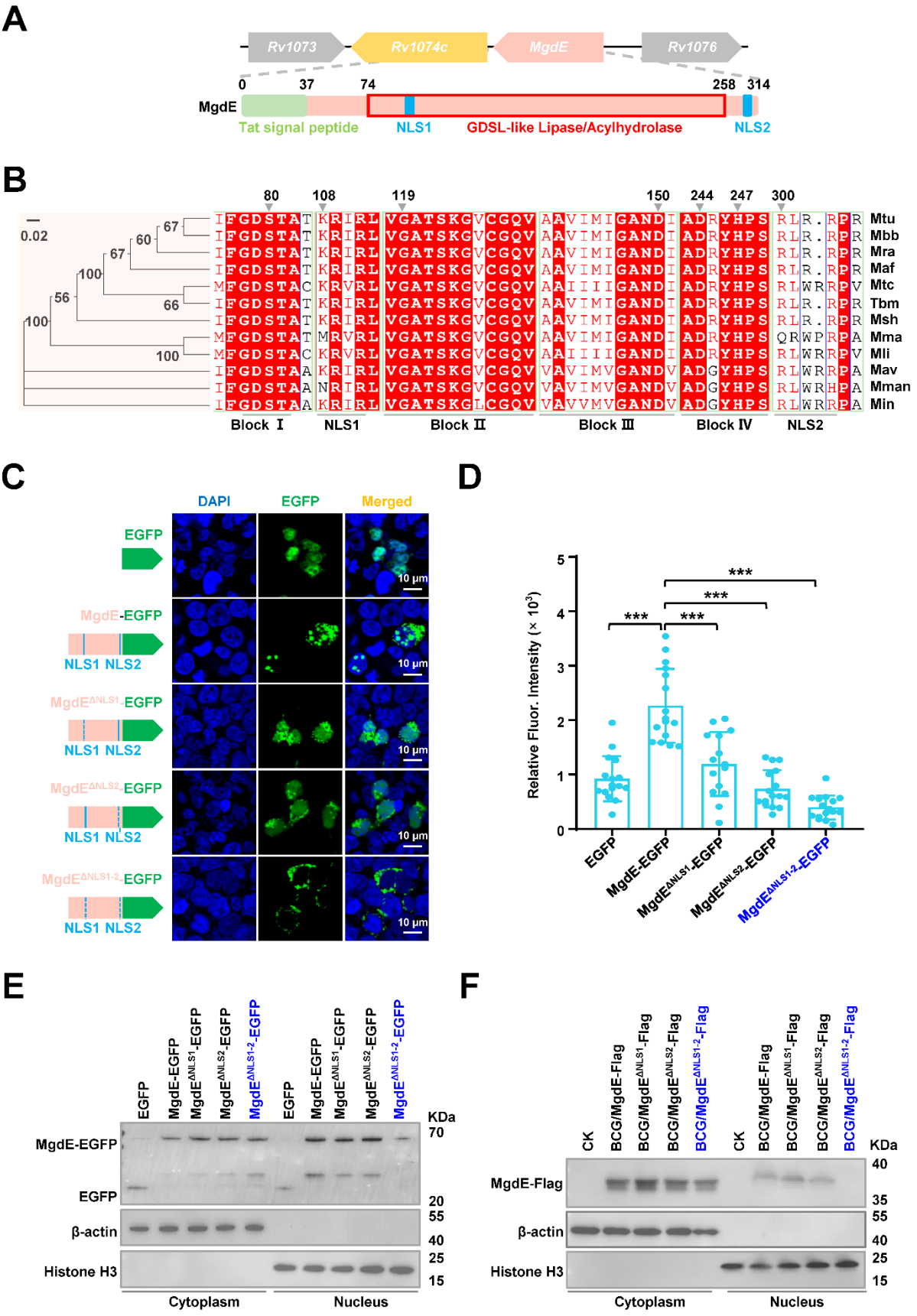

Figure 2. Hypothetical protein MgdE enters the host nucleus via dual NLS.

(**A**) Domain architecture of MgdE. Schematic representation of MgdE with the annotated functional domains, including a Tat signal peptide (1–37 aa, twin-arginine translocation motif), a GDSL-like lipase/acylhydrolase catalytic domain (74–258 aa), and two nuclear localization signals (NLS1: 108–111 aa, NLS2: 300–305 aa). (**B**) Phylogenetic and structural conservation of MgdE. (left) Neighbor–joining phylogenetic tree of MgdE homologs across Mycobacterium species (1,000 bootstrap replicates, values ≥50% shown). (right) Clustal Omega sequence alignment highlighting conserved residues (≥90% identity, red). Species abbreviations: *M. tuberculosis* (Mtu), *M. bovis* BCG (Mbb), *M. tuberculosis* H37Ra (Mra), *M. africanum* (Maf), *M. tuberculosis* CDC1551 (Mtc), *M. tuberculosis* GM041182 (Tbm), *M. shinjukuense* (Msh), *M. marinum* (Mma), *M. lupini* (Mli), *M. avium* (Mav), *M. manitobense* (Mman), *M. intracellulare* (Min). **(C)** Subcellular localization of EGFP-tagged wild-type MgdE and its NLS-deletion mutants ($MgdE^{\Delta NLS1}$, $MgdE^{\Delta NLS2}$, and $MgdE^{\Delta NLS1\text{-}2}$). (left) Schematic representation of EGFP-tagged constructs. (right) Representative confocal microscopy images of HEK293T cells transfected with the indicated constructs for 36 h. EGFP fluorescence (green) and nuclear staining with DAPI (blue) were visualized using FLUOVIEW software (v5.0). Scale bar, 10 μm. Images were acquired using a 100× oil immersion objective (NA = 1.4). (**D**) Quantification of nuclear EGFP intensity in cells expressing wild-type or mutant MgdE constructs. Data are presented as mean ± SD (n = 15 cells). Statistical significance was assessed by two-tailed unpaired Student's *t*-tests (***$P < 0.001$). (**E**) Western blot analysis of nuclear and cytoplasmic fractions from HEK293T cells transfected with wild-type MgdE and its NLS-deletion mutants. The empty EGFP vector was used as a negative control. EGFP and MgdE-EGFP fusion proteins were detected using an anti-GFP antibody. Histone H3 and β-actin served as nuclear

812 and cytoplasmic markers, respectively. **(F)** Nuclear localization of MgdE during infection. THP-
813 1 macrophages were infected with recombinant *M. bovis* BCG strains expressing Flag-tagged
814 wild-type MgdE or NLS-deletion mutants ($MgdE^{\Delta NLS1}$, $MgdE^{\Delta NLS2}$, and $MgdE^{\Delta NLS1\text{-}2}$) for 24
815 hours. Subcellular fractionation was performed, and cytoplasmic and nuclear fractions were
816 analyzed by immunoblotting using anti-Flag antibodies. Histone H3 and β-actin were used as
817 nuclear and cytoplasmic markers, respectively.
818

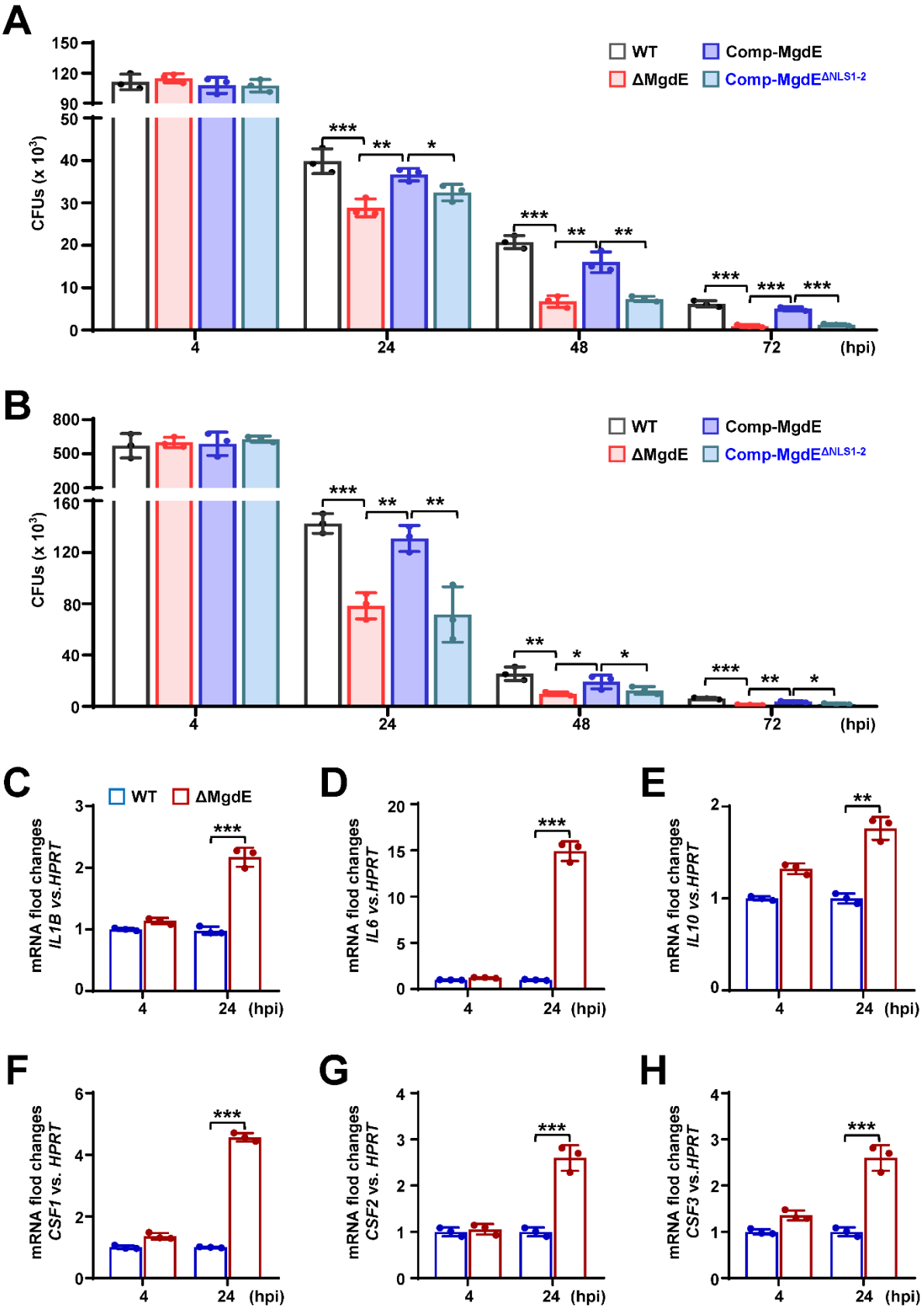

819

820 **Figure 3. Nuclear localization of MgdE facilitates mycobacterial intracellular survival in**

821 **macrophages.**

822 (**A**–**B**) Intracellular survival of *M. bovis* BCG strains. THP-1 human macrophages (**A**) and
823 RAW264.7 murine macrophages (**B**) were infected (MOI = 10) with wild-type BCG (WT), MgdE
824 deletion mutant (ΔMgdE), complemented strain (Comp-MgdE), or NLS-deficient complement
825 (Comp-MgdE$^{\Delta NLS1\text{-}2}$). Bacterial survival was assessed by CFU enumeration at 2, 24, 48, and
826 72 h post-infection. (**C–H**) Cytokine expression in the infected THP-1 cells. qRT-PCR analysis
827 of cytokine mRNA levels in THP-1 cells infected with WT or ΔMgdE strains for 4–24 h. Target
828 genes include *IL1B* (**C**), *IL6* (**D**), *IL10* (**E**), *CSF1* (**F**), *CSF2* (**G**), and *CSF3* (**H**). Data are
829 presented as mean ±SD of three biologically independent experiments, analyzed using two-
830 tailed unpaired Student's *t*-tests (**P* < 0.05, ***P* < 0.01, and ****P* < 0.001).

831

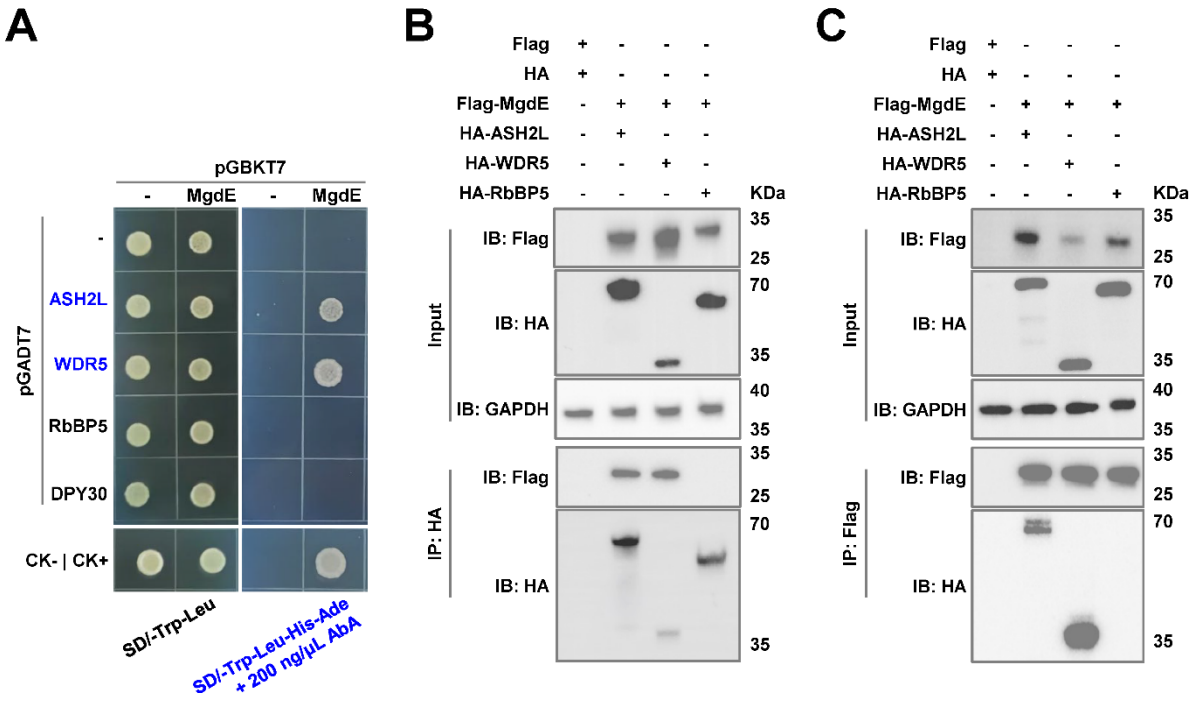

832

833 **Figure 4. MgdE directly interacts with ASH2L and WDR5, core components of the host**
834 **COMPASS complex.**

835 (**A**) Yeast cells were co-transformed with bait (pGBKT7) and prey (pGADT7) plasmids
836 expressing wild-type MgdE and human COMPASS components (ASH2L, WDR5, RbBP5, and
837 DPY30). Growth was monitored on non-selective (-Leu/-Trp, left) and selective (-Leu/-Trp/-
838 Ade/-His + 200 ng/μL aureobasidin A, right) media. Controls: CK− (pGBKT7-*lam* + pGADT7-
839 T, negative), CK+ (pGBKT7-*p53* + pGADT7-T, positive). (**B**–**C**) Cells were co-transfected with
840 Flag-MgdE and HA-tagged ASH2L, WDR5, or RbBP5 (1:1 molar ratio). At 36 h post-
841 transfection, the lysates were immunoprecipitated using (**B**) anti-HA or (**C**) anti-Flag antibodies,
842 followed by immunoblotting with anti-HA, anti-Flag, and anti-GAPDH (loading control). The
843 input lanes represent 5% of the total lysate.
844

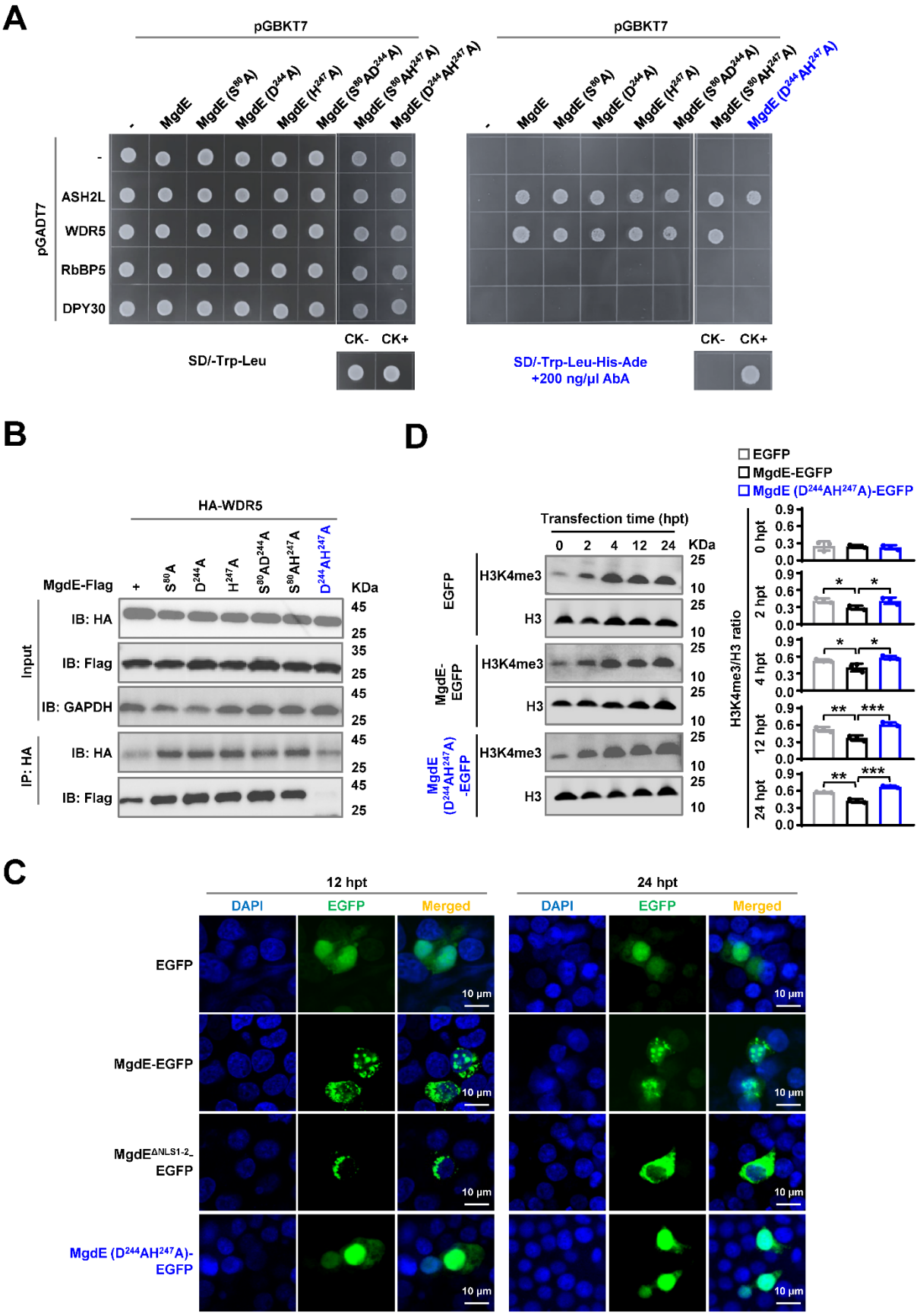

845

846 **Figure 5. The conserved residues D^{224} and H^{247} mediate the binding ability of MgdE to**

847 **WDR5.**

848 (**A**) Y2H assay identifying interactions between MgdE mutants and COMPASS complex
849 subunits. Yeast cells were co-transformed with bait (pGBKT7) and prey (pGADT7) plasmids
850 expressing wild-type or mutant MgdE and human COMPASS subunits (ASH2L, WDR5,
851 RbBP5, and DPY30). Growth was assessed on non-selective (-Leu/-Trp, left) and selective (-
852 Leu/-Trp/-Ade/-His + 200 ng/μL aureobasidin A, right) media. Controls: CK− (pGBKT7-*lam* +
853 pGADT7-T, negative) and CK+ (pGBKT7-*p53* + pGADT7-T, positive). (**B**) Co-IP analysis of
854 MgdE mutants with WDR5. HEK293T cells were co-transfected with Flag-tagged MgdE
855 mutants and HA-tagged WDR5 (1:1 molar ratio). Complexes were immunoprecipitated using
856 anti-HA antibody and protein A/G beads, followed by immunoblotting with anti-Flag and anti-
857 HA antibodies. (**C**) Nuclear distribution of wild-type and mutants MgdE. Confocal microscopy
858 of HEK293T cells expressing wild-type or $D^{224}A/H^{247}A$ MgdE-EGFP at 12 and 24 h post-
859 transfection (hpt). Nuclear foci were visualized by EGFP (green) and DAPI (blue) staining.
860 Scale bar, 10 μm. Images were acquired with a ×100 oil immersion objective (NA = 1.4). (**D**)
861 Immunoblot analysis of H3K4me3 levels. HEK293T cells expressing wild-type or $D^{224}A/H^{247}A$
862 mutant MgdE were analyzed for changes in H3K4me3 levels over 0–24 h post-transfection.
863 Histone H3 was used as a loading control. The data represent three independent biological
864 replicates.

865

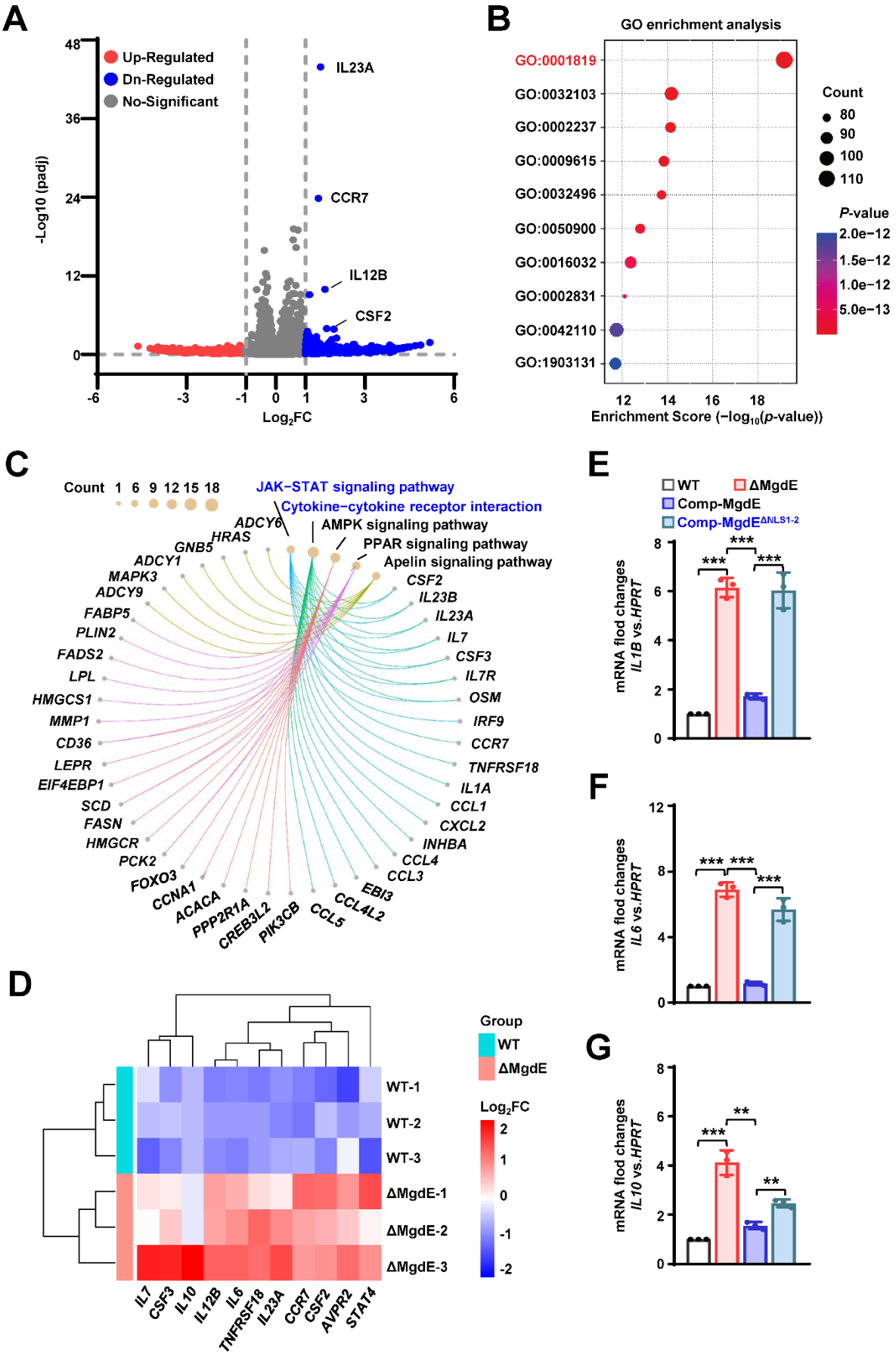
A
Up-Regulated
Dn-Regulated
No-Significant
IL23A
CCR7
IL12B
CSF2
-Log10 (padj)
Log2FC
B
GO enrichment analysis
GO:0001819
GO:0032103
GO:0002237
GO:0009615
GO:0032496
GO:0050900
GO:0016032
GO:0002831
GO:0042110
GO:1903131
Count
P-value
Enrichment Score (−log10(p-value))
C
Count
JAK-STAT signaling pathway
Cytokine-cytokine receptor interaction
AMPK signaling pathway
PPAR signaling pathway
Apelin signaling pathway
D
Group
WT
ΔMgdE
Log2FC
WT-1
WT-2
WT-3
ΔMgdE-1
ΔMgdE-2
ΔMgdE-3
IL7
CSF3
IL10
IL12B
IL6
TNFRSF18
IL23A
CCR7
CSF2
AVPR2
STAT4
E
WT
ΔMgdE
Comp-MgdE
Comp-MgdEΔNLS1-2
mRNA flod changes IL1B vs.HPRT
F
mRNA flod changes IL6 vs.HPRT
G
mRNA flod changes IL10 vs.HPRT

867 **Figure 6. MgdE suppresses host inflammatory responses probably by inhibition of**
868 **COMPASS complex-mediated H3K4 methylation.**

869 (**A**) Volcano plot of DEGs. DEGs between MgdE-deleted strain (ΔMgdE) and wild-type BCG
870 (WT) were visualized in a volcano plot. Genes with $|\log_2\text{-fold change}| \geq 1$ and $P < 0.05$ were
871 considered significant. The *x*-axis represents $\log_2$fold change, and the *y*-axis shows $-\log_{10}(P$-
872 value). (**B**) GO enrichment analysis of DEGs. GO analysis revealed the significant enrichment
873 of immune and inflammatory processes in ΔMgdE-infected macrophages compared to that in
874 WT-infected cells, including positive regulation of response to external stimulus (GO:0032103),
875 response to molecule of bacterial origin (GO:0002237), response to virus (GO:0009615),
876 response to lipopolysaccharide (GO:0032496), leukocyte migration (GO:0050900), viral
877 process (GO:0016032), regulation of response to biotic stimulus (GO:0002831), T cell
878 activation (GO:0042110), and mononuclear cell differentiation (GO:1903131). (**C**) KEGG
879 pathway enrichment analysis of DEGs. Chord diagram of KEGG pathway enrichment analysis
880 showing signaling pathways that are significantly enriched in ΔMgdE. (**D**) Heatmap of the
881 inflammatory gene expression. Heatmap depicting $\log_2$-foldchange levels of inflammatory
882 genes involved in the JAK–STAT and cytokine signaling pathways. Upregulated and
883 downregulated genes in ΔMgdE are shown in green and red, respectively. The data were *Z*-
884 score normalized. (**E-G**) qRT-PCR analysis of cytokine mRNA levels in THP-1 cells infected
885 with WT, ΔMgdE, MgdE-complemented (Comp-MgdE), and NLS-deleted complement (Comp-
886 $\text{MgdE}^{\Delta\text{NLS1-2}}$) at 24 h post-infection. Cytokines analyzed include *IL1B* (**E**), *IL6* (**F**), and *IL10* (**G**).
887 Data are presented as mean ± SD of three biologically independent experiments, analyzed
888 using two-tailed unpaired Student's *t*-tests (*$P < 0.05$, **$P < 0.01$, and ***$P < 0.001$).

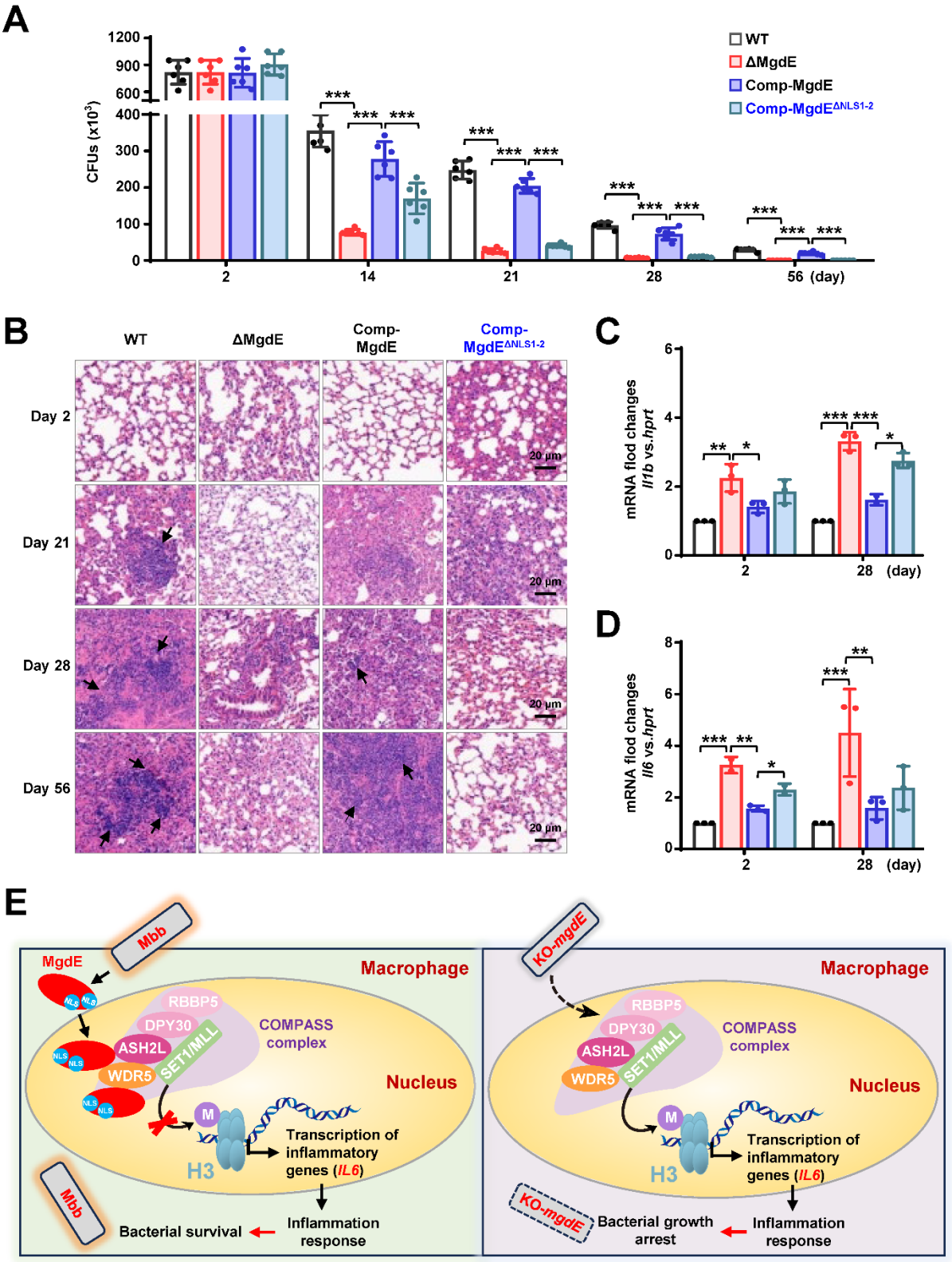

Figure 7. Nuclear localization of MgdE is essential for mycobacterial survival in mice.

(**A**) Bacterial burden in the lungs of the infected mice. C57BL/6 mice (n = 6/group) maintained

892 under SPF conditions were intratracheally infected with 1.0 × 10^7 colony-forming units (CFU)
893 of *M. bovis* BCG strains, including wild-type (WT), MgdE-deleted (ΔMgdE), MgdE-
894 complemented (Comp-MgdE), and NLS-deleted complement (Comp-MgdE$^{\Delta NLS1\text{-}2}$). Lung
895 bacterial loads were quantified using CFU assays at 0, 14, 21, 28, and 56 d post-infection. (**B**)
896 H&E-stained lung sections from infected mice (as in **A**) revealed granulomatous inflammation.
897 Scale bars: 200 μm. (**C–D**) Pro-inflammatory cytokine expression in mice spleen. qRT-PCR
898 analysis of cytokine mRNA levels of *Il1b* (**C**) and *Il6* (**D**) in spleen tissues from infected mice
899 (n = 6/group) at 2 and 28 days post-infection. Data are presented as mean ± SD from six
900 biologically independent experiments. Statistical significance was determined by a two-tailed
901 unpaired Student's *t*-test (**P* < 0.05, ***P* < 0.01, and ****P* < 0.001). (**E**) Mechanistic model
902 showing how mycobacterial nucleomodulin MgdE hijacks the COMPASS complex to suppress
903 H3K4me3 and promote immune evasion. Upon *M. bovis* BCG infection, the nucleomodulin
904 MgdE is delivered into the host nucleus via its nuclear localization signal (NLS) and directly
905 binds to the COMPASS complex subunits, ASH2L or WDR5. This interaction disrupts H3K4
906 trimethylation (H3K4me3) deposition, leading to the epigenetic suppression of pro-
907 inflammatory cytokine transcription (e.g., *IL6*), thereby facilitating the intracellular survival of
908 the pathogen.

909 **Supplementary figures**

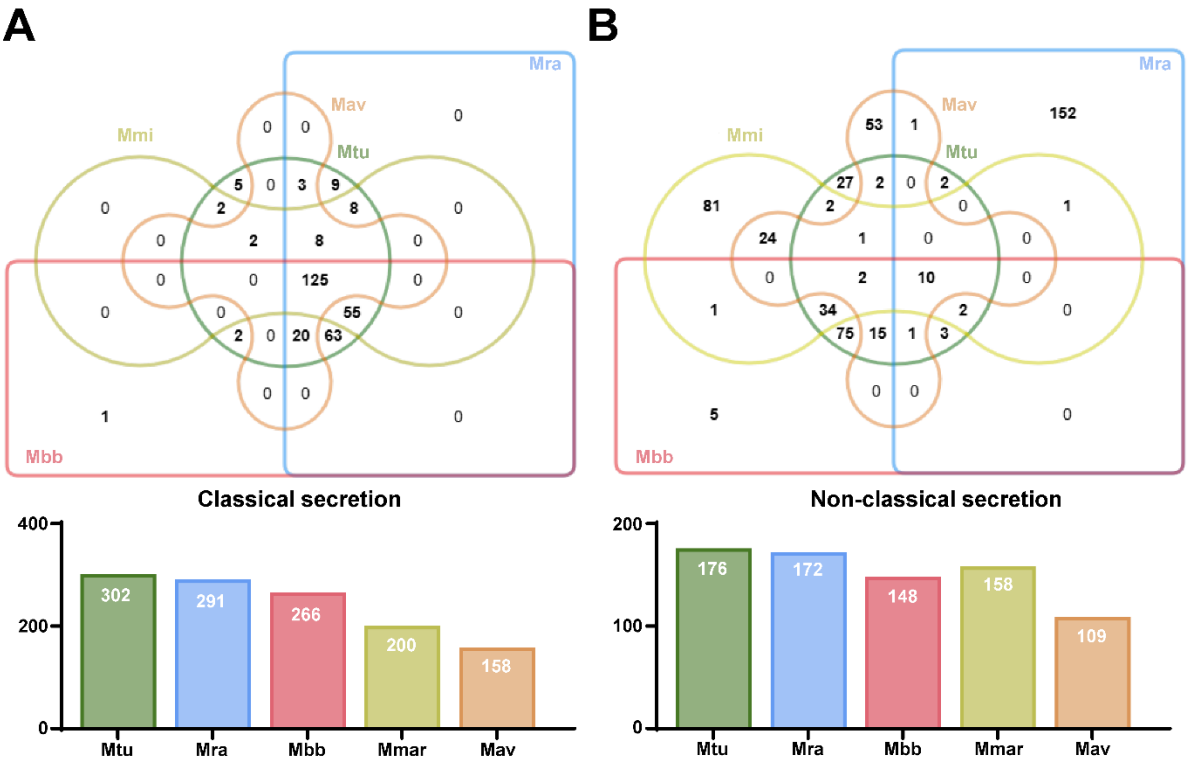

910

911 **Supplementary figure 1. Comparative analysis of classical and non-classical secreted**

912 **proteins in mycobacterial species.**

913 (**A**) Venn diagram showing the distribution of predicted classical secreted proteins in four

914 Mycobacterium species: *M. tuberculosis* H37Rv (Mtu) and *M. tuberculosis* H37Ra (Mra), *M.*

915 *bovis* BCG (Mbb), *M. marinum* (Mmar), and *M. avium* (Mav). Proteins were predicted using

916 SignalP 5.0, with a signal peptide score (D-score) ≥ 0.5. A total of 125 proteins were conserved

917 across all species. (**B**) Venn diagram showing the distribution of predicted non-classical

918 secreted proteins across the same Mycobacterium species, predicted using SecretomeP 2.0

919 with a neural network (NN) score ≥ 0.9. Ten proteins were conserved across all species. Bar

920 graphs (left: classical, right: non-classical) summarize the total number of predicted secreted

921 proteins per species.

922

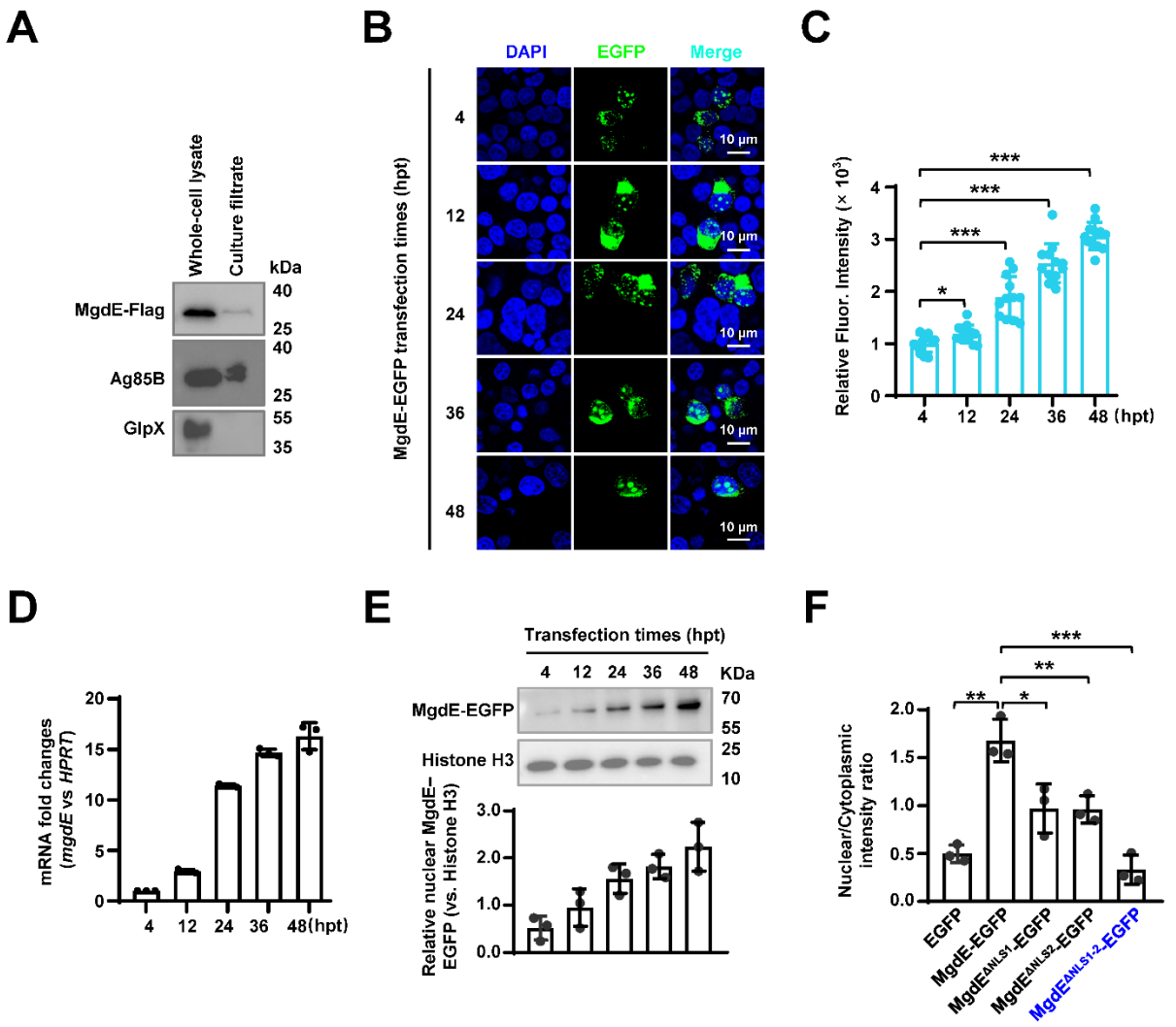

Supplementary Figure 2. Subnuclear localization of MgdE-EGFP.

(**A**) Immunoblot analysis of bacterial lysates and culture supernatants from *M. bovis* BCG strains expressing C-terminally Flag-tagged MgdE. Endogenous Ag85B and GlpX were detected using anti-Ag85B and anti-GlpX antibodies, serving as positive and negative controls for protein secretion, respectively. MgdE-Flag was detected using an anti-Flag antibody. (**B**) Confocal microscopy was used to assess the nuclear distribution of MgdE-EGFP at various time points post-transfection. Nuclei were stained with DAPI (blue), MgdE-EGFP is shown in green. Scale bar: 10 μm. Images were acquired using a 100× oil immersion objective (NA = 1.4). **(C)** Quantification of nuclear EGFP intensity in cells expressing wild-type or mutant MgdE

933 constructs. Data are presented as mean ± SD (n = 12 cells). (**D**) Quantitative RT-PCR analysis
934 of *mgdE* mRNA expression in HEK293T cells at different time points post-transfection (4–48
935 h). Data represent the transcriptional level of *mgdE* relative to *HPRT*. (**E**) Western blot analysis
936 of nuclear fractions at different time points post-transfection (4–48 h), showing time-dependent
937 nuclear accumulation of MgdE-EGFP. Histone H3 was used as a loading control for nuclear
938 proteins. The lower panel shows quantification of nuclear MgdE-EGFP levels normalized to
939 Histone H3. Data are presented as mean ± SD (n = 3). (**F**) Quantification of the nuclear and
940 cytoplasmic distribution of EGFP, wild-type MgdE, and its NLS-deletion mutants based on the
941 Western blot results shown in (**Figure 2E**).

942

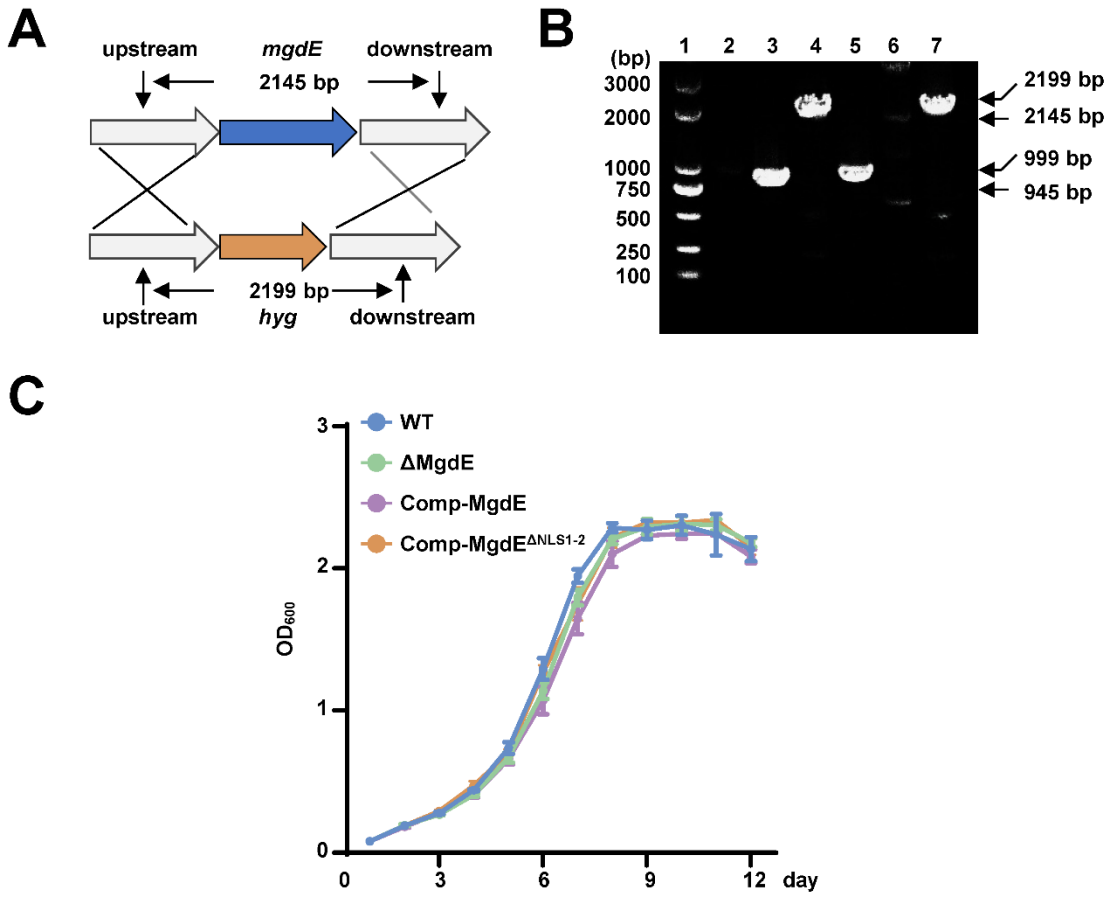

943

944 **Supplementary Figure 3. Deletion of the nuclear localization signal of MgdE does not**

945 **affect the growth of *M. bovis* BCG strains.**

946 (**A-B**) Construction and validation of the MgdE-deleted strain of *M. bovis* BCG. (**A**) Schematic
947 diagram of the homologous recombination strategy used to delete *mgdE* from the *M. bovis*
948 BCG genome. (**B**) Wild-type and mutant strains were used as templates to amplify the *mgdE*
949 gene (600 bp upstream–600 bp downstream) by PCR. Lanes 1 and 3: wild-type genomic DNA,
950 lanes 2 and 4: Δ*mgdE* genomic DNA. (**C**) Growth curve analysis of *M. bovis* BCG strains.
951 Growth of BCG strains, including wild-type BCG (WT), MgdE-deleted (ΔMgdE), MgdE-
952 complemented (Comp-MgdE), and NLS-deleted complemented (Comp-MgdE$^{\Delta NLS1\text{-}2}$) strains,
953 was measured in 7H9 medium.

A

Function	COMPASS complexes	Predicted binding confidence (pLDDT)
The catalytic subunit	SET1A/B	-
Required for H3K4me3	ASH2L	0.47
Required for assembly	RBBP5	0.30
Required for assembly	WDR5	0.77
	DPY30	0.62
Components of the Set1 complexes	CXXC1	0.51
	WDR82	-
Components of the Set1 complexes	HCF1	0.37

B

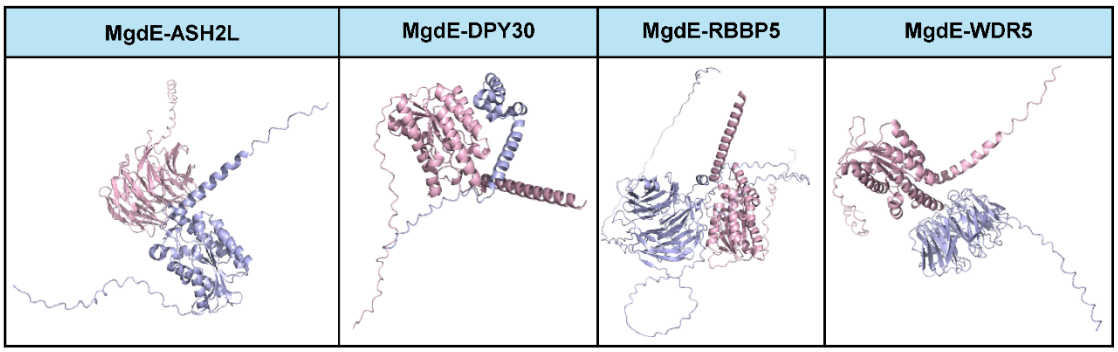

C

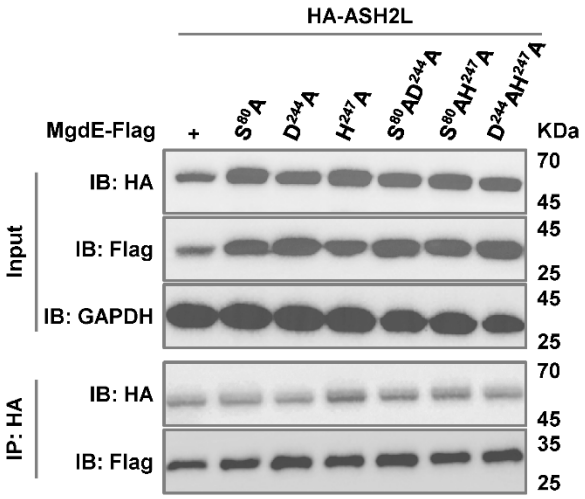

954

955 **Supplementary Figure 4. MgdE interacts with COMPASS complex subunits.**

956 (**A**) Predicted binding affinities between MgdE and COMPASS core subunits. The predicted

957 local distance difference test (pLDDT) scores calculated using AlphaFold 2.2.0 for the

interactions between MgdE and the COMPASS subunits were as follows: ASH2L (pLDDT = 0.47), RbBP5 (pLDDT = 0.30), WDR5 (pLDDT = 0.77), and DPY30 (pLDDT = 0.62). Confidence levels are categorized as follows: High confidence: pLDDT ≥ 0.7 (strong predicted binding), Medium confidence: 0.5 ≤ pLDDT < 0.7 (moderate binding), Low confidence: pLDDT < 0.5 (weak predicted binding). (**B**) Structural modeling of MgdE-COMPASS interactions. AlphaFold generated models of the simulated binding interfaces are shown, with MgdE highlighted in red and COMPASS subunits (ASH2L, WDR5, RbBP5, and DPY30) shown in gray. (**C**) Co-IP analysis of MgdE mutants with ASH2L. HEK293T cells were co-transfected with Flag-tagged MgdE mutants and HA-tagged ASH2L (1:1 molar ratio). Co-IP was performed using anti-HA antibody-bound protein A/G beads, and immunoprecipitated complexes were analyzed by immunoblotting with anti-Flag and anti-HA antibodies.

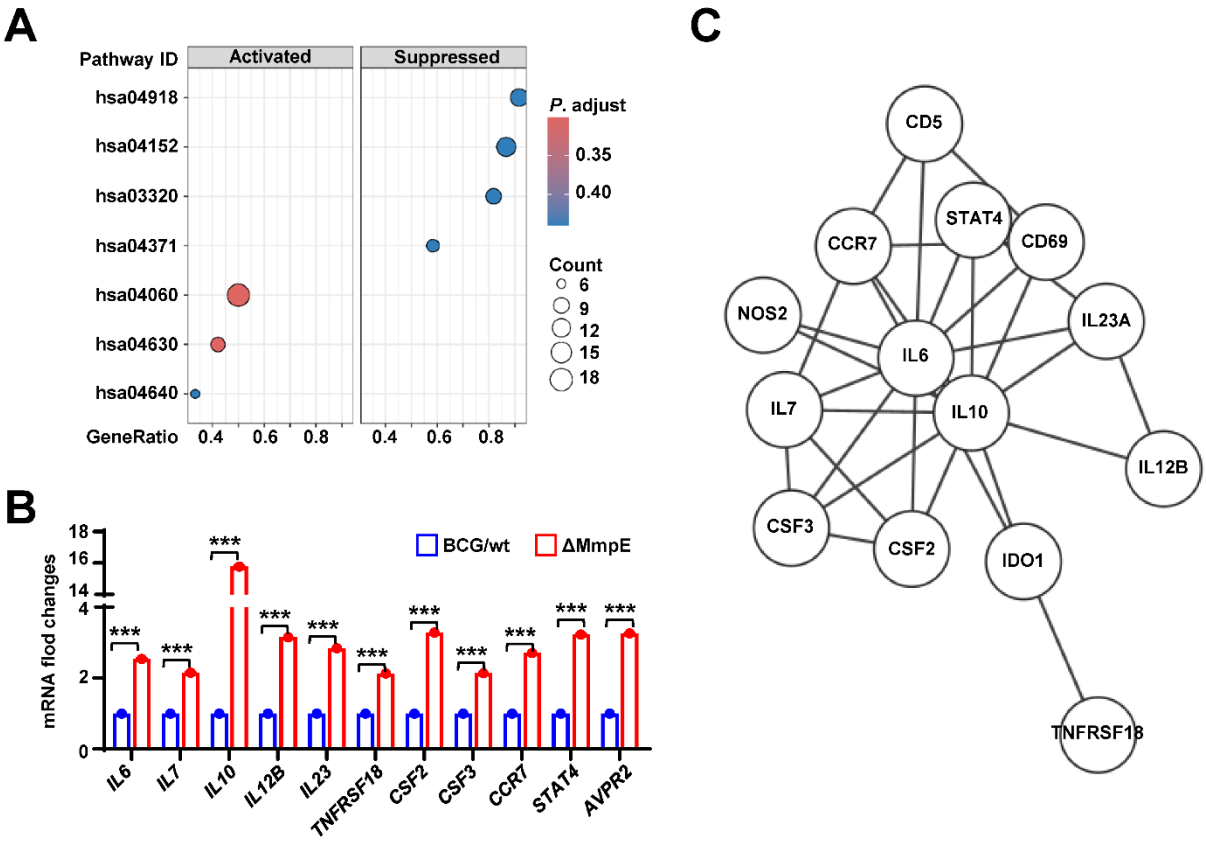

971 **Supplementary Figure 5. MgdE suppresses cellular inflammatory responses during *M.***

972 ***bovis* BCG infection.**

973 (**A**) KEGG pathway enrichment analysis. KEGG pathway analysis identified significantly

974 enriched pathways in THP-1 cells infected with the ΔMgdE strain compared to those infected

975 with wild-type BCG (WT). DEGs were predominantly associated with immune and signaling

976 pathways, including thyroid hormone synthesis (hsa04918), AMPK signaling pathway

977 (hsa04152), PPAR signaling pathway (hsa03320), apelin signaling pathway (hsa04371),

978 Cytokine–cytokine receptor interaction (hsa04060), JAK–STAT signaling pathway (hsa04630),

979 and hematopoietic cell lineage (hsa04640). (**B**) Elevated inflammatory gene expression in

980 ΔMgdE-infected cells. Key upregulated inflammatory genes in ΔMgdE- *vs*. WT-infected cells

981 are highlighted. (**C**) Functional enrichment analysis of upregulated genes. Analysis using

982 STRING and Cytoscape revealed regulation of inflammatory responses as a top enriched

983 biological process ($P < 0.05$).

984

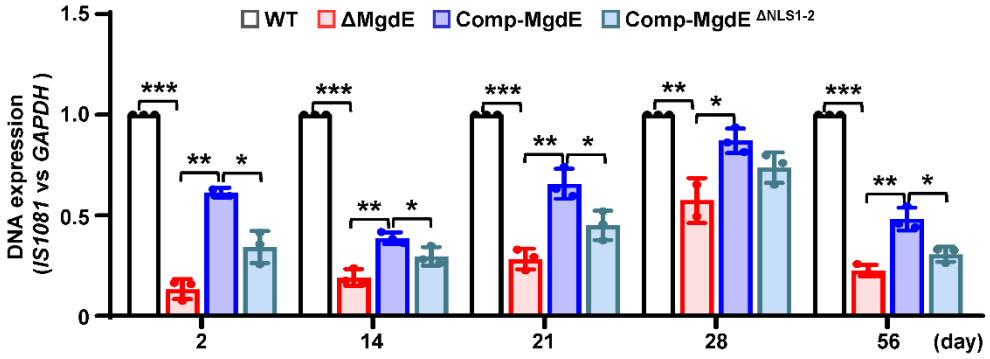

985

986 **Supplementary Figure 6. MgdE facilitates bacterial colonization in the spleens of**

987 **infected mice.**

988 Bacterial colonization was assessed in splenic homogenates from infected mice (as described

989 in **Figure 7A**) by quantifying bacterial DNA using quantitative PCR at 2, 14, 21, 28, and 56

990 days post-infection. Data are presented as mean ± SD (n = 3). Statistical significance was

991 determined using a two-tailed unpaired Student's *t*-test ($P < 0.05$, $^{**}P < 0.01$, and $^{***}P < 0.001$).

992